Evolution of shear zones through the brittle-ductile transition: the Calamita Schists (Elba Island, Italy).

Samuele PAPESCHI[a,b,*], Giovanni MUSUMECI[b,c] and Francesco MAZZARINI[c]

a. Dipartimento di Scienze della Terra, Firenze University, via la Pira 4, 50121 Firenze, Italy

b. Dipartimento di Scienze della Terra, Pisa University, via Santa Maria 53, 56126 Pisa, Italy

c. Istituto Nazionale di Geofisica e Vulcanologia, via della Faggiola 32, 56126 Pisa, Italy

***Corresponding author:**

Primary e-mail: s.papeschi@gmail.com

Institutional e-mail: Samuele.papeschi@unifi.it

Phone: +393202472057

Address: Dipartimento di Scienze della Terra, via Santa Maria 53, 56126 Pisa (PI), Italy.

Authors' e-mails:

Giovanni Musumeci: giovanni.musumeci@unipi.it

Francesco Mazzarini: francesco.mazzarini@ingv.it

Keywords: brittle-ductile transition; mylonite; shear zone; shear band; faulting; strain localization.

Abstract

A network of shear zones that evolved through the brittle-ductile transition is exposed in the Calamita Schists, Elba Island, Italy. The shear zones formed during Late Miocene contractional deformation coeval with high grade contact metamorphism (~650 °C) related to the emplacement of plutonic rocks at shallow crustal levels (~7-10 Km). An early stage high metamorphic grade foliation was overprinted by mylonitic deformation that progressively localized on low-metamorphic grade shear bands producing S-C mylonites during cooling of contact aureole.

Localization of deformation on shear bands was driven by temperature decrease that triggered strain partitioning between 'hard' high grade relics and 'soft' shear bands. Softening of shear bands occurred likely due to fluid influx and retrograde growth of fine-grained phyllosilicates. The interconnection of anastomosing shear bands and passive rotation of the relic high grade foliation caused widening of the shear bands producing mylonites with a composite mylonitic foliation and C' shear bands. An estimate of the vorticity number Wk of the flow of ~0.3 – 0.5 was obtained from the orientation of C' shear bands measured at the meso- and thin section-scale. Close to the brittle-ductile transition, the growth of soft phyllosilicates allowed C' shear bands to act as precursory structures to brittle deformation localized into an array of low-angle faults and shear fractures.

1. Introduction

Shear zones are tabular high-strain zones localized within domains of relatively lower strain that accommodate deformation in the lithosphere (Ramsay and Graham, 1970; Sibson, 1977; Ramsay, 1980; Lister and Snoke, 1984). They are usually distinguished in plastic (ductile or viscous) or brittle shear zones, according to their dominant deformation mechanism (Fossen and Cavalcante, 2017). However, brittle and ductile deformation mechanisms interplay during deformation, accompanying nucleation, growth and evolution of shear zones (e.g. Fusseis et al., 2006; Pennacchioni and Mancktelow, 2007; Fusseis and Handy, 2008). The transition from brittle to ductile behaviour differs from mineral to mineral and depends in first order on the temperature of deformation (Sibson, 1983; Hirth and Tullis, 1994; Gleason and Tullis, 1995). Temperature is also the critical parameter that controls dislocation creep regimes (Hirth and Tullis, 1992; Stipp et al., 2002), as well as fluid reactivity and metamorphic reactions (Bucher and Grapes, 2011). At high grade (T>600 °C), only unusual dry conditions (Jackson et al., 2004; Gerald et al., 2006; Menegon et al., 2011) or high strain rates (e.g. Gleason and Tullis, 1995) enhance rock strength favouring brittle deformation, like in the case of pseudotachylites reported in the lower crust (Austrheim and Boundy, 1994; Menegon et al., 2017). In the vast majority of cases, high-temperature shear zones are dominated by crystal plastic deformation, with silicates, like quartz and feldspars, forming elongate 'ribbon grains' that define the foliation (White et al., 1980; Gapais, 1989; Hippertt et al., 2001; Rosenberg and Stünitz, 2003). Moreover, under high temperature conditions, the average grain size tends to be coarse as dynamic recrystallization occurs by grain boundary migration (Stipp et al., 2002). Strain partitioning is quite uncommon, as large rock volumes deform by low flow stress and therefore high grade shear zones tend to be thick and characterized by a continuous mesoscale foliation (Passchier and Coelho, 2006).

At medium to low grade (300 °C < T < 600 °C), shear zones exhibit a more complex behaviour. Competency contrasts between different lithologies becomes important and results in heterogeneous deformation of rocks with strain partitioning between rheologically 'strong' and 'weak' domains (Passchier and Coelho, 2006). Some minerals (e.g. quartz) deform by dislocation creep while others (e.g. feldspar) may undergo brittle fracturing or deform by grain size sensitive mechanisms (e.g. Tullis et al., 1982; Menegon et al., 2013; Viegas et al., 2016). As a consequence, shearing localizes and produces complex arrays of shear zones (Pennacchioni, 2005; Fusseis et al., 2006; Carreras et al., 2010) that bounds volumes of relatively low-strain (lozenges; Ponce et al., 2013). Shear zones themselves show internal strain partitioning highlighted by the presence of shear band structures (Berthé et al., 1979) that localize shearing obliquely to the co-existing mylonitic foliation (S). Shear bands are distinguished in relatively straight and continuous C shear bands, elongated parallel to the shear zone boundary, and short and closely spaced at the mm- to the cm-scale C' shear bands that develop obliquely in respect to the shear zone boundary (Berthé et al., 1979; White, 1979; Lister and Snoke, 1984), alternatively known as extensional crenulation cleavage (Platt and Vissers, 1980). Conjugate sets of C' shear bands with opposite sense of shear, synthetic and antithetic respectively, may sometimes be developed in response to the bulk shear zone flow (Law et al., 2004; Little et al., 2011; Gillam et al., 2014). Deformation in shear zones is characterized by a strong grain size reduction, which has itself been regarded as an efficient strain softening mechanism (White et al., 1980; Kilian et al., 2011; Platt, 2015). The formation of a lattice preferred orientation, allowing slip on the 'softer' slip system (Rutter et al., 2001; Ji et al., 2004) or substitution of 'strong' phases with a mixture of 'soft' grains by metamorphic reaction (Steffen et al., 2001; Stünitz and Tullis, 2001), also contribute to keep deformation localized within discrete shear zones at low- to medium grade conditions. As the offset and strain increase, shear zone thicken at the expenses of low-strain domains (Means, 1995). This has been documented in several natural examples (e.g. Tauern window: Pennacchioni and Mancktelow, 2007; Cap de Creus: Fusseis et al., 2006) and related to the linkage of several shear zone segments that cut through the wall rock. Strain hardening of the shear zone core (caused by the growth of 'strong' phases, the accumulation of dislocations or softening of the walls) commonly occurs promoting widening of shear zones (Fossen and Cavalcante, 2017).

Especially at low-grade conditions (i.e. shallow crustal levels), slight changes in temperature may cause swings in deformation mechanisms and influence how deformation is partitioned within the shear zone. An example is represented by the Glarus thrust in the Swiss Alps, that developed at shallow crustal levels accommodating over 50 Km of displacement and localizing deformation in ~1 metre of mylonites. During thrust activity, temperature decrease led to a narrowing of the shear zone in the fault core with the later development of brittle cataclastic bands parallel to the shear zone walls (Ebert et al., 2007). In the South Armorican Shear Zone, one of the major tectonic lineaments of the Variscan chain, shearing produced mylonites with shear bands (Berthé et al., 1979). Bukovskà et al. (2016) showed that, while the main mylonitic foliation formed at around ~550 °C, shear bands developed at ~300-350 °C. These authors also documented the progressive widening of shear bands, aided by microcracking that promotes fluid infiltration and reaction softening. As a result deformation progressively localizes on shear bands that are oblique to the mylonitic foliation. The importance of strain partitioning at the brittle/ductile transition may indeed dramatically increase as brittle structures are superimposed onto a pre-existing ductile fabric. Brittle structures may localize parallel to the shear zone walls, as in the case of the Glarus thrust (Ebert et al., 2007) or take advantage of precursory shear bands and oblique structures nucleating in unlikely orientations in respect to the typical ‘Andersonian’ faults of Anderson (1951). Failure along pre-existing foliations has been documented in several metamorphic units (Butler et al., 2008; Massironi et al., 2011; Bistacchi et al., 2012) and related to the low-friction coefficient of ‘weak’ phyllosilicates aligned on foliations (Zhang and He, 2016).

In this study we present a detailed meso- and microscale analysis of shear zones, evolved from ductile to brittle conditions within the high- to medium- metamorphic grade Calamita Schists in southeastern Elba Island (Italy). Shearing in the Calamita Schists has been imposed by contractional tectonics, coeval with pluton emplacement at very shallow (< 7 Km) crustal level (e.g., Papeschi et al., 2017). The transition from high-temperature to low-temperature deformation has been determined by the relatively rapid (< 1 Ma) cooling of the metamorphic rocks hosting the monzogranite (Musumeci and Vaselli, 2012). We highlight the role of shear bands in localizing deformation from high-temperature to low-temperature conditions and in promoting the switch to the brittle regime, where shear bands have acted as ductile precursors for brittle, non-Andersonian faults.

2. Geological setting

In the northern Tyrrhenian Sea, Elba Island exposes a complete structural section of the hinterland sector of the northern Apennines belt (Boccaletti et al., 1971) that recorded early to late Miocene nappe stacking and late Miocene contractional deformation coeval with emplacement of intrusive rocks (Pertusati et al., 1993; Keller and Coward, 1996; Massa et al., 2017).

The Elba Island nappe stack consists of non-metamorphic and metamorphic tectonic units (Keller and Coward, 1996) separated by a major thrust fault (Capo Norsi thrust; CNT in Fig. 1), into an Upper and a Lower Complex (Musumeci and Vaselli, 2012). The Upper Complex is characterized by non-metamorphic ocean-derived units on top of very low-grade continental units (see Massa et al., 2017 for a detailed description). The Lower Complex consists of two continent-derived metamorphic units, the Ortano Unit and the underlying Calamita Unit, which are characterized by

Paleozoic metasediments and metavolcanics (Musumeci et al., 2011) and Mesozoic age siliciclastic and carbonate metasediments (Fig. 1).

The Lower Complex features early Miocene blueschist to greenschist facies metamorphism (Bianco et al., 2015), which has been deeply overprinted by late Miocene low-pressure/high-temperature (LP/HT) metamorphism in the amphibole to pyroxene hornfels facies (Musumeci and Vaselli, 2012), dated between 6.7 and 6.2 Ma (Musumeci et al., 2011, 2015). Peak metamorphic conditions in the Lower Complex exceeded 650 °C at pressures below 0.18-0.20 GPa (Duranti et al., 1992). LP/HT metamorphism has been related to the emplacement of the Porto Azzurro pluton, which is buried at ~150-200 metres beneath the Calamita peninsula (Musumeci et al., 2015) and exposed only as scattered outcrops of monzogranite (Fig. 1). Furthermore, tourmaline-bearing leucogranite and pegmatite dykes (Eastern Elba dyke complex; Mazzarini and Musumeci, 2008) widely crop out in the eastern sector of the Calamita peninsula (Fig. 1). Available radiometric ages of the outcropping magmatic products range between 6.33±0.07 Ma (leucogranite dyke; Musumeci et al., 2015) and 5.9±0.2 Ma (monzogranite; Maineri et al., 2003).

Pluton emplacement and LP/HT related metamorphism were coeval with late Miocene regional scale east-verging shortening, testified by (i) thrust shear zones (Calanchiole shear zone and Felciaio shear zone; CSZ and FSZ in Fig.1; Musumeci and Vaselli, 2012) and (ii) a kilometre-scale upright antiform of foliation (Ripalte antiform; Fig. 1), cored by high-grade metamorphic rocks and leucogranites (Mazzarini et al., 2011).

All the tectonic structures of the nappe stack and the late Miocene intrusive rocks in the Lower complex, were crosscut by the Zuccale fault (ZF in Fig. 1; Collettini and Holdsworth, 2004; Smith et al., 2011; Musumeci et al., 2015), whose activity postdated igneous rocks emplacement and cooling. Debate involves the interpretation of the ZF as a detachment or a thrust (see discussion in Musumeci et al., 2015). According to the former interpretation, the ZF would represent the main extensional structure, while according to the latter interpretation, the ZF would constitute the roof thrust of a large scale late Miocene duplex structure affecting the whole eastern Elba nappe stack (see Fig. 13 in Papeschi et al., 2017).

3. The Calamita Unit

3.1. Metamorphism and structural setting

The Calamita Unit, host of the Porto Azzurro pluton (Fig. 1), consists of interlayered schists and metapsammites of Early Carboniferous age (Calamita Schists Fm.) overlain by Triassic metasiliciclastics (Barabarca quartzite Fm.) and metacarbonates (Calanchiole marble Fm.). Andalusite + cordierite + K-feldspar + biotite ± white mica in the Calamita Schists and diopside + tremolite assemblages in the Calanchiole marble indicate temperatures between 500 and 600 °C (Musumeci and Vaselli, 2012) with peak metamorphic conditions exceeding 650 °C at pressures below 0.18-0.20 GPa (Duranti et al., 1992). At map scale, the peak metamorphic assemblage allows to distinguish a white mica + biotite + cordierite + andalusite zone on the western side of the Calamita peninsula and a biotite + K-feldspar + cordierite + andalusite zone on the eastern side. Common retrograde phases include white mica, sericite and chlorite.

The Calamita Schists are characterized by localized high-strain domains (HSDs), developed during Late Miocene deformation and heterogeneously distributed at map scale, that display a continuous foliation associated with shear bands (Papeschi et al., 2017). HSDs are characterized by: i) N-S striking and moderately (10-40°) W-dipping foliation, ii) E-W trending stretching and mineralogical lineations, iii) constant top to the east/northeast sense of shear and iv) east-verging low angle brittle faults that cross cut the main schistosity (0-15° eastward dip). At the microscale, quartz fabric in HSDs outlines an evolution of deformation mechanisms from grain boundary migration to bulging recrystallization that has been interpreted as indicative of progressive temperature decrease during deformation (Papeschi et al., 2017).

In the following paragraphs we focus on the meso- and microscale fabric of HSDs, investigated in two different sections, namely (i) the Capo Calvo HSD (Fig. 2a) and (ii) the Praticciolo HSD (Fig.

4a), that are characterized by different fabrics and located on the eastern and western limb of the Ripalte antiform respectively (location in Fig. 1). Details about the samples investigated in these sections are provided in Appendix A.

4. High temperature ductile fabric: Capo Calvo section

4.1. Mesostructures

At Capo Calvo, the Calamita Schists crop out as high metamorphic grade metapsammites (biotite + andalusite + cordierite + K-feldspar) intruded by leucogranite and pegmatite dykes (Fig. 2a).

The dominant mesoscale fabric is a high grade metamorphic foliation (Sp) that strikes N140-160 and dips moderately (20-50°) to the northeast (Fig. 2a). Mineral lineations are defined by aggregates of quartz and biotite and by the preferred orientation of andalusite, cordierite and K-feldspar: they trend about N050-N090 and plunge to the northeast (Fig. 2a).

The Sp is defined by alternations of well foliated biotite-rich and stretched quartz-rich layers that wrap around weakly foliated biotite-andalusite-cordierite-bearing lozenges, whose asymmetric shape is consistent with top to the east sense of shear (Fig. 2b). The Sp is cross cut at low angle (20-30°) by top to the east C and C' shear bands (Fig. 2b) defining an S/C fabric in which the Sp corresponds to the oblique S foliation (Fig. 2b). C shear bands dip moderately (20 - 50°; Fig. 2a) towards the east and are characterized by thickness from few millimetres up to some centimetres and spacing ranging from several centimetres up to some decimetres. C' shear bands are characterized by steep eastward dip (between 40 and 80°; Fig. 2a) and make an angle of ~10-15° with C shear bands. They are discontinuous and characterized by millimetric thickness and a spacing of several centimetres.

C shear bands, defined by thin, stretched micaceous and quartzitic layers, form an array of interconnected medium- to fine-grained shear planes with areas of linkage and wrap centimetric to millimetric lozenges with an oblique S foliation (Fig. 2b). In the most strained domains, C shear bands evolve in a well developed mylonitic foliation (Sm) characterized by subparallel quartz- and mica-rich layers enveloping boudinated andalusite-cordierite-biotite pods (Fig. 2c). The Sp foliation in the walls is dragged into parallelism with the Sm, consistently with top to the east sense of shear. Steeply east dipping top to the east C' shear bands with centimetric spacing cross-cut the Sm (Fig. 2c).

4.2. Microstructures

At the microscale, the main foliation (Sp) is defined by alternations of millimetric quartz ribbons and thin biotite-rich layers or elongated quartz grains with trails of biotite (Fig. 3a). The Sp wraps lenses of diablastic aggregates characterized by intergrown coarse -grained (500 μm – 2 mm) euhedral andalusite and cordierite, commonly altered in fine-grained sericite, biotite and K-feldspar with poikiloblastic biotite inclusions (Fig. 3b).

Quartz occurs as coarse (~500 μm) grains showing interlobate to amoeboid grain boundaries with island grains (Jessel, 1987) and patchy undulose extinction. When associated to other phases, commonly biotite, pinning microstructures (Passchier and Trouw, 2005), indicative of fast grain boundary migration (e.g. Stipp et al., 2002, 2010), are common (Fig. 3a). Finer quartz grains (<100 μm) with ellipsoidal shape occur as bulges along grain boundaries, showing roughly the same size as coarse quartz grains subgrains.

At the contact with C shear bands, the oblique Sp foliation consists of quartz ribbons and lepidoblastic coarse-grained biotite bands (Fig. 3d) that wrap coarse-grained (up to 5 mm) diablastic aggregates of biotite, K-feldspar, andalusite and cordierite. Coarse quartz grains display undulose extinction and are mantled by fine-grained (10-100 μm) interlobate quartz aggregates (Fig. 3d). Biotite shows kinks and wide extinction bands that are roughly perpendicular to the basal cleavage planes. Sericite ribbons, elongated parallel to the Sp foliation, wrap porphyroclast of andalusite, cordierite and K-feldspar.

The transition between the Sp foliation and C shear bands (Fig. 3c) is marked by an abrupt grain size decrease associated with the shear drag of the oblique Sp foliation in parallelism with C planes

(Fig. 3e). Dragged quartz and biotite ribbons are marked by a grain size reduction from 500 µm -1 mm to few tens of micrometres in correspondence of the transition zone (Fig. 3e).

C planes display a very fine-grained mylonitic foliation characterized by interlayered thin, stretched quartz ribbons and very fine-grained (<10 µm) lepidoblastic sericite-biotite-chlorite aggregates. Quartz ribbons consists of very tiny (<20 µm) equigranular grains with slightly interlobate boundaries and undulose extinction. Ellipsoidal aggregates of sericite, sized 100-200 µm and wrapped by the C foliation, represent pseudomorphs over relic andalusite and cordierite grains. The mylonitic foliation is dragged with top to the east sense of shear along micrometric C' shear bands, with a spacing of some hundreds of microns, marked by very fine-grained phyllosilicates.

In quartz-rich layers, the Sp foliation is defined by interlobate aggregates of coarse old grains (100-500 µm) and finer (~50 µm) new grains, both showing a strong preferred orientation (Fig. 3f). New grains are characterized by less elongate elliptical shape and occur associated with subgrains and small bulges of similar size and shape. C shear bands are filled with mixtures of very fine grained chlorite and sericite that abruptly interrupts the S foliation (Fig. 3f).

5. Praticciolo: medium to low-temperature ductile-brittle fabric

5.1. Mesostructures

The Praticciolo cape, located at the southwestern tip of the Calamita peninsula, (Fig. 1) exposes medium metamorphic grade rocks of the Calamita Schists and Calanchiole marble (Fig. 4a). This latter discordantly overlies the Calamita Schists over a low-angle east-dipping fault zone (Figs. 4a, b; Papeschi et al., 2017). The Calamita Schists consists of white mica + biotite + andalusite + cordierite ± chlorite bearing schists and quartzites, while the Calanchiole marble is mostly made of impure and dolomitic marbles with diopside-tremolite-talc-phlogopite paragenesis interlayered with tremolite-talc phyllites.

The main foliation (Sp) in the Calamita Schists strikes N-S and dips towards the west at ~30-40° (Fig. 5a). Mineral lineations, outlined by quartz and biotite aggregates and cordierite and andalusite coarse grains trend east-west and plunge to the west (Fig. 5a). The Calamita Schists are characterized by a strain gradient from weakly foliated schist (low-strain domain) in the northeast to well foliated schists (high-strain domain) in the southwest (Fig. 4b). At outcrop scale, the high strain domain is characterized by decimetre- to metre-thick bands of S-C' with a west/southwest dipping mylonitic foliation (Sm; Fig. 5a) defined by alternations of stretched quartzite layers and mylonitic biotite-andalusite-bearing schists (Fig. 5c). The mylonitic foliation is displaced by gently east- to west-dipping millimetre-thick C' shear bands that are characterized by top to the east sense of shear (Fig. 5a). They show variable spacing, ranging from few millimetres in mylonitic schists, up to centimetres/decimetres in thick quartzite layers (Fig. 5c). Quartzite layers display shear band boudinage and are offset along C' shear bands with displacements of few millimetres up to some centimetres (Fig. 5c). A second set of steep, C' antithetic west-verging shear bands is sometimes present in thick and coarse quartzite layers wrapped by the Sm, where it intersect synthetic east-verging C' shear bands at closely orthogonal angle (Fig. 5d).

The mylonitic fabric is cross-cut by a network of shear fractures and low-angle east dipping faults (0-15°; Fig. 5b). Faults are characterized by decimetric to metric eastward displacements and feature a banded cataclastic core zone made up of centimetre-thick unfoliated cataclasite and millimetre-thick foliated ultracataclasite (see below, Fig. 7a). Slickenlines are defined by quartz fibres trending about east-west (Fig. 5b). Shear fractures define a pattern of Riedel shears that, following Logan et al. (1992), correspond to east-verging (i) gently east dipping (0-15°) Y shear fractures, (ii) moderately east dipping (10-30°) synthetic R1 shear fractures and antithetic west-verging (iii) steep (40-70°) R2 shear fractures (Fig. 5b). Displacements range from 1-2 millimetres to some centimetres. This Riedel shear geometry is overall consistent with eastward directed sense of shear. At outcrop scale, a parallelism exists between discrete C' shear bands (Fig. 5c) and Y shear fractures (Fig. 5e). Y shear fractures are often localized on C' shear bands separating boudins of quartz-rich layers (Fig. 5e). R1 shear fractures form en-echelon arrays that connect Y shear fracture segments in step over areas, allowing the linkage between parallel Y shears segments (Fig.

5f). Intense damage zones, with a thickness of few centimetres up to decimetres, appear to be characterized by multiple Y, R1 and R2 shear fracture segments that dissect angular blocks of Calamita Schists. In damage zones, Riedel shears - in particular R2 shear fractures - locally exhibit decimetric displacements sometimes cross cutting low-angle fault zones (e.g. Fig. 11a in Papeschi et al., 2017).

5.2. Microstructures

The mylonitic foliation (Sm) is defined by interlayered lepidoblastic mica domains (Fig. 6a) and quartz ribbons (Fig. 6b). Mica domains feature fine-grained (<50 μm) white micas characterized by a strong shape preferred orientation, that are locally dragged along east-verging C' shear bands (Fig. 6a). Micas wrap andalusite and cordierite porphyroclasts (200 - 500 μm) and diablastic aggregates of coarse-grained biotite, andalusite and cordierite elongated parallel to the mylonitic foliation. In many cases, andalusite and cordierite grains are substituted by fine-grained aggregates of chlorite and sericite elongated parallel to the Sm (Fig. 6b). Biotite is commonly pseudomorphosed by chlorite.

Quartz is characterized by a strongly heterogeneous microfabric. Large, coarse-grained (>500 μm) old quartz grains constitute the cores of large ribbons and boudins (Fig. 6b). They are wrapped by finely recrystallized (~10-100 μm) new quartz grains, produced by subgrain rotation and bulging recrystallization (Fig. 6b) (Papeschi et al., 2017). New grains of uniform grain size are arranged in ribbons stretched parallel to the Sm (Fig. 6b). They show amoeboid to interlobate boundaries and a moderate shape preferred orientation parallel to the Sm. Large areas of ribbons appear extinct at the same time, indicating the presence of a CPO (Fig. 6b). Old quartz grains, which occupy the core of quartz ribbons, are characterized by linear to interlobate grain boundaries with small, localized bulges and recrystallized tiny, new quartz grains (Fig. 6b, d). Grains showing amoeboid boundaries, island grains and reticulate microstructures are locally present as relics largely overprinted by new grains nucleated by subgrain rotation recrystallization. Patchy to undulose extinction patterns (Figs.

6d, e) with fine and wide extinction bands (sensu Derez et al., 2015) are common within coarse quartz grains.

Networks of synthetic (Fig. 6d) and antithetic (Fig. 6e) C' shear bands pass through old quartz grains forming discrete, brittle shear fractures, decorated by trails of very fine-grained (~10 μm) quartz grains and phyllosilicates (sericite and chlorite) with a preferred orientation parallel to the shear bands (Fig. 6c). Synthetic C' shear bands show eastward sense of shear, making a moderate ~20-30° angle in respect to the Sm (Fig. 6d). The antithetic set of C' shear bands shows westward sense of shear and is locally present in thick quartz ribbons where it forms a set of shear fractures conjugate with synthetic shear bands that are closely orthogonal (Fig. 6e). Irregular patterns of fractures with very limited or null slip are associated with conjugate sets of shear bands (Fig. 6e), localized in coarse quartz and quickly dying out when they enter fine-grained quartz ribbons or mica-rich domains.

Low-angle faults, occurring parallel to C' shear bands (Fig. 7a), are characterized by a layered microfabric with a foliated ultracataclasite band localized at the contact with the hanging wall block and an unfoliated cataclasite band lying below, closer to the footwall block (Fig. 7b). In the wall rocks, mylonitic deformation features are overprinted by low-grade recrystallization microstructures. Coarse-grained interlobate and amoeboid quartz grains, deformed by grain boundary migration recrystallization, are mantled by aggregates of very fine-grained (< 20 μm) quartz grains (Fig. 7c). Trails of very fine-grained quartz define conjugate bands that cross cut coarse quartz grains (Fig. 7c). Shear fractures, filled by a very fine-grained mixture of phyllosilicates, occur inclined to the main fault plane (Fig. 7c). The contact between the wall rock and the ultracataclasite is marked by a millimetre-thick mass of very finely recrystallized (< 10 μm) quartz which contains sparse, relic, old quartz grains (Fig. 7d). These latters display conjugate sets of very fine-grained quartz trails, whose shape preferred orientation is oblique to the fault wall (Fig. 7d). Sharp shear fractures locally penetrate from the ultracataclasite into the wall rock enveloping recrystallized angular fragments of quartzite. The main foliation (Cf) in the ultracataclasite is outlined by trails of angular wall rock fragments and by coloured bands of sericite and brownish phyllosilicate which represent the cataclasite matrix (Fig. 7e). The cataclastic foliation disappears in the underlying cataclastic band, where the microfabric is characterized by heterometric angular fragments of quartz with microstructures similar to the wall rocks, wrapped by an unfoliated, brownish phyllosilicate-rich matrix.

6. Shear band analysis in the Calamita Unit

The attitudes of Sp/Sm foliations and C' shear bands have been measured at outcrop scale at Capo Calvo and the Praticciolo. The Fisher (1959) mean vector to the pole of each measured structural element has been calculated using Stereonet 10 (Allmendinger, 2005). Additional details are available in Appendix A.

The angular relationships between foliations (Sp, Sm) and shear bands (C, C') have been also evaluated at the microscale by measuring their relative orientation and their dihedral angles, on a sample from Capo Calvo and 4 samples from the Praticciolo (summary in Tab. 1 and additional details in Appendix A). In the sample from Capo Calvo, the relative orientations of the S, C and C' foliations have been evaluated using the analyze particles routine of the software ImageJ (Schneider et al., 2012) and plotted in rose diagrams using the software OpenStereo (Grohmann and Campania, 2010), where the reference line (E-W diameter) corresponds to the average orientation of C shear bands in the field. The S/C and C/C' dihedral angles at Capo Calvo and the Sm/C' dihedral angles at the Praticciolo have been measured directly with the angle tool of the ImageJ software.

6.1 Results of shear bands measurements

At Capo Calvo the mean pole to the Sp foliation is 240.9/57.2±12.0° (1σ) and the average pole to C' shear bands is 242.5/37.1±12.8° (Tab. 1). The average Sp/C' acute dihedral angle is 37.1±8.7. Thin section scale measurements on the Capo Calvo sample (Fig. 8a) provide an average Sp/C' dihedral angle of 41.9±4.6°, an Sp/C dihedral angle of 21.1±4.6° and a C/C' dihedral angle of

15.2±1.9° (Tab. 1). At the Praticciolo cape, the mesoscale Sm foliation has a mean pole of 79.2/56.9±15.1° while the average pole to C' shear bands is oriented at 70.5/87.1±9.1° (synthetic C') and 47.3/18.2±39.5° (antithetic C'). The average acute dihedral angle between Sm and synthetic C' shears corresponds to 30.2±8.8° and the average obtuse dihedral angle between synthetic and antithetic C' shear bands is 110.9±20.3° (Tab. 1). Similar values of Sm/C' dihedral angles have been obtained from the thin section measurements, ranging between 31.2±3.1° (minimum) and 38.4±3.7° (maximum) (Tab. 1).

Figure 8 shows an example of the angular relationships between foliation and shear bands from the Capo Calvo sample. The sample displays the contact between high grade schists with Sp foliation and a mylonitic centimetre-thick C shear band (Fig. 8a). C shear bands define a strong maximum with 52% of the C planes measurements oriented close to the sample horizontal, while Sp foliation planes appear more scattered (Fig. 8b). Based on microstructural observations, we observed a progressive decrease of the Sp/C dihedral angle within the lozenge approaching the contact with the C shear band (Fig. 8a). Therefore we distinguished three subdomains: (i) the wall rock, (ii) the Sp/C contact, corresponding to the area within 1 centimetre from the contact with the C shear band (Fig. 8a) and (iii) the C shear band itself, where the Sp foliation is not present. Within the wall rock subdomain the mean Sp/C dihedral angle is 36.7±2.4° (Fig. 8c) whereas in the Sp/C contact subdomain the mean Sp/C dihedral angle is reduced to just 21.1±3.4° and Sp and C orientations locally overlaps (Fig. 8d). This highlights the progressive decrease of the Sp/C dihedral angle approaching the C shear band subdomain. In the latter, the Sp is not present and C' shear bands, oriented at ~15° in respect to C shear bands (Fig. 8e) occur.

7. Discussion

7.1. Shear zones in the Calamita Unit: geometry and evolution

The studied sections in the Calamita Unit represent an example in which deformation evolves in a very short time span (~ 800 Ky; Musumeci et al., 2015) from metre to decametre-thick ductile high-strain domains to narrow and localized brittle shear zones (Papeschi et al., 2017). Deformation occurred during cooling of metamorphic rocks at low pressure conditions (<0.18-0.20 GPa). Assuming (i) an uplift/erosion rate between 1 and 2 mm/yr and (ii) an average density of 2.7 g/cm^3 a vertical exhumation of 800 - 1600 metres, (0.02-0.04 GPa) can be estimated and therefore pressure can be considered nearly constant during deformation.

The earlier fabric, represented by a high grade metamorphic foliation, has been overprinted by shear bands (Fig. 9a). At peak metamorphic conditions (600-650 °C), fast grain boundary migration, recorded within coarse grained quartz ribbons, allows deformation to be distributed within high strain domains. Grain boundary migration was likely promoted by fluid circulation, which in the examined high metamorphic grade metapelites can derive from (i) dehydratation metamorphic reactions (i.e. muscovite-out reaction; Pattison and Tracy, 1992) and (ii) hydrothermal fluids originated from the host igneous rocks (Porto Azzurro pluton and felsic dykes; Dini et al., 2008).

The transition to C shear bands (Fig. 9a) is marked by (i) a sharp decrease in grain size (Fig. 3c, e, f) and (ii) the widespread growth of sericite-chlorite bearing metamorphic assemblages (Fig. 3c, e). These latters occurs as retrograde alteration of previous mineral assemblage (i.e. andalusite, cordierite and K-feldspar) and indicates low temperature conditions (T<400-450 °C) and circulation of intragranular water-rich fluids.

High-temperature quartz microstructures are overprinted by new quartz grains resulting from low- to medium- temperature bulging and subgrain rotation recrystallization (Stipp et al., 2002), as already suggested by Papeschi et al. (2017). Evidence of subgrain rotation recrystallization is highlighted by the oblique orientation of new quartz grains with respect to C shear bands orientation (Fig. 3f), recrystallizing along the extensional instantaneous stretching axis of the flow (Law et al., 1984; Wallis, 1995). In the most deformed domains C shear bands evolve to mylonitic shear zones with a continuous mylonitic foliation (Fig. 9b), characterized by fine-grained quartz ribbons and mixed quartz-sericite layers (e.g. Fig. 3e). Strain hardening of the quartzo-feldspathic domains (i.e. relic high grade foliation) outside and/or enveloped by shear bands (Fig. 9a) favoured strain localization during temperature decrease into C shear bands, via reaction softening with fluid influx and growth of soft phyllosilicates (e.g. Stunitz and Tullis, 2001; Jessel et al., 2009; Bukovskà et al., 2016), enhancing grain size sensitive creep (Kilian et al., 2011; Viegas et al., 2016). The decrease of the Sp/C dihedral angles and the parallelism between the two foliations at the shear zone boundary (Fig. 8c, d) indicate a passive rotation of the Sp foliation towards the orientation of C shear bands. A similar evolution has been documented by Berthé et al. (1979) in the South Armorican Shear Zone, where they observed decrease of dihedral angles with increasing strain and the reactivation of the S foliation as C shear planes. Therefore, the evolution from localized shear bands (Fig. 9a) to wider shear zones with a well developed mylonitic foliation (Fig. 9c) has been accomplished by (i) passive rotation and deformation of the high grade Sp foliation and (ii) linkage of anastomosing shear zones that coalesced and consumed low-strain domains, similarly to the Cap de Creus example described by Fusseis et al. (2006).

The mylonitic foliation is overprinted by discontinuous C' shear bands (Fig. 9c). In phyllosilicate-rich domains C' shear bands are characterized by the shear drag of mica and chlorite grains (Fig. 6a), suggesting that they formed by re-orientating pre-existing phyllosilicates parallel to the shear band itself (e.g. Jessel et al., 2009). On the other hand, in competent layers (i.e. thick and coarse-grained quartz ribbons) C' shear bands form oppositely verging conjugate sets (Fig. 6e) marked by fine-grained phyllosilicates indicative of low temperature conditions (T<400 °C). The incipient stage of C' shear band development is marked by trails of very fine-grained (~10 μm) new quartz grains (Fig. 6e), which might indicate low temperature bulging recrystallization. The development of conjugate shear bands in coarse quartz grains (Fig. 6e) might be related to the increasing effect of competency contrast at low temperature conditions (greenschist facies), driving strain hardening of 'coarse and stiff' quartz grains (e.g. Menegon et al., 2008). Patterns of fractures, associated with C' shear bands, indicate that they formed by brittle mechanisms. Thus coarse quartz grains experienced a progressive embrittlement while the surrounding fine grained mylonitic foliation (quartz new grains and phyllosilicates) was still deforming in a ductile way. The growth of phyllosilicates and fine-grained quartz on C’ shear bands could have been produced by low temperature recrystallization and/or precipitation from a fluid phase, as shown by Kjøll et al. (2015).

These features, from a natural example, are consistent with the nucleation of C’ shear bands as a consequence of rheological heterogeneities as shown by the experimental data of Holyoke and Tullis (2006) and the numerical model of Jessel et al. (2009).

7.2. Brittle-ductile transition: shear fractures and role of precursory shear bands.

The entirely-brittle stage of shear zone activity is evidenced by Y shear fractures parallel to C’ shear bands (Fig. 9d) and subsidiary shear fractures that outline a network of R1 and R2 Riedel shears consistent with top to the east sense of shear parallel to the ductile direction of tectonic transport (Fig. 5a, b). Moreover some fault zones, parallel to Y shear fractures (Fig. 5b), preserve in their wall rocks trails and aggregates of very fine quartz grains (Fig. 7c, d). These microstructures are cross cut by brittle shear fractures and are preserved in angular quartz-rich clasts embedded in the cataclasite (Fig. 9b), indicating that low temperature recrystallization occurred before brittle failure. These features may be consistent with nucleation of faults and shear fractures close to the brittle-ductile transition with low temperature recrystallization overprinted by brittle deformation.

The strict relationships between C’ shear bands and Y shear fractures, highlighted by their parallelism (Fig. 5a, b) and the observed localization of Y shears in correspondence of C’ shear bands (Fig. 5e), suggest that C’ shear bands acted as precursors for Y shear fractures. At the microscale, C’ shear bands in competent domains bear evidence of recrystallization associated to brittle fracturing (e.g. Fig. 6e). This latter can be considered the incipient stage of fracture propagation at the brittle-ductile transition. The brittle reactivation of C’ shear bands could be favoured by the presence of low-friction coefficient phyllosilicates (Zhang and He, 2016). Differently, the main mylonitic foliation (Sm), although characterized by fine-grained sericite layers (e.g. Fig. 6b), does not show any evidence of brittle reactivation. This feature could be related to the different orientation of shear bands and the Sm with respect to the maximum stress (σ1) in the brittle regime. R1 and R2 shears are active simultaneously with Y shears (Logan et al., 1992), therefore the paleo-orientation of σ1 (i.e. the bisector plane of the mean conjugate R1 and R2 shears; Fig. 10a) can be estimated. The calculated mean σ1 direction is oriented 97.3/38.2±19.1° and σ3 at 267.3/51.8±19.1°. The σ1 orientation lies makes a ~30-40° angle with the average orientation of C' shear bands (dip/dipdir: 03/250) and is roughly orthogonal to the Sm foliation (33/261) (Fig. 10a). Slip tendency analyses have been performed using the program FaultKin (Allmendinger et al., 1992), assuming zero pore fluid pressure and the same coefficient of static friction μ for the Sm foliation and shear bands. Several values of μ, between 0.2 and 0.7, have been used at varying conditions of differential stress (10-150 Mpa) to evaluate the slip tendency Ts (Morris et al., 1996). In Fig. 10b the slip tendency analysis for C' shear bands and the Sm foliations is shown for a μ value of 0.45 and a differential stress of 80 MPa. Under these conditions, C' shear bands display the highest probability to reactivate (red circles in Fig. 10b) whereas the Sm foliation show low slip tendency (cyan circles in Fig. 10b). These values fit well with the observed natural structures. Slip on the Sm foliation can be promoted by increasing the differential stress and/or the pore fluid pressure or by decreasing the μ coefficient. Thus, differential stress and the coefficient of static friction exert a strong control over the reactivation of ductile precursors and hence over the geometries of brittle structures. The favourable orientation for brittle reactivation of C' shear bands can be visualized by plotting the average orientation of C' shear bands and the Sm on the Mohr circle (Fig. 10c). In this example two cohesion-less failure envelopes have been plotted, one for general failure (μ=0.7) and the other for failure along shear bands/foliation (μ=0.45). Although in this example both C' shear bands and the Sm are equally weak (μ=0.45), the Sm is so unfavourably oriented in respect to σ1 that failure takes place across the foliation (R1 shears) (Fig. 10c).

This situation is similar to the experiments on sheared foliated rocks performed by Ikari et al. (2015) on a foliated black slate at various orientations in respect to the applied shear stress. In the experimental setting with foliation dipping in the opposite direction in respect to the shear sense (Fig. 10d), these authors observed the early nucleation of R1 shears across the foliation. Failure along the foliation occurs only at higher shear stresses with the formation of foliation-parallel P shears (Fig. 10d). These authors concluded that under these conditions the main foliation is unfavourably oriented for slip and therefore R1 shears are forced to form from early stages of deformation (see also Sibson, 1985; Collettini and Sibson, 2001).

We suggest that the high strain domain in the Calamita Schists represent a natural analogue of the experiment of Ikari et al. (2015). In respect to the experiments of Ikari et al. (2015), the presence of a second set of weakness planes, represented by C' shear bands, might have caused the early localization of deformation onto precursory C' shear bands, producing networks of Y and R1 shears. This might have also inhibited the reactivation of the foliation ì, which has been observed by Ikari et al. (2015). Therefore we propose that at the brittle-ductile transition deformation switched progressively from the well developed mylonitic foliation into discordant networks of shear fractures that formed as a consequence of the reactivation of precursory shear bands in the brittle regime.

7.3 Shear zone flow and shear band orientation.

The orientation of C' shear bands within a shear zone is thought to be related to the degree of non-coaxiality of the shear zone (Law et al., 2004) and can be used to estimate the vorticity of the flow (Kurz and Northrup, 2008).

At the Praticciolo, the mean dihedral angle between the Sm and C' shear bands measured at the mesoscale (30.2±8.8°) overlaps with the ~30-38° values (Tab. 1) calculated at thin section scale. This suggests that C' shear bands lie on average at a constant orientation and they have not significantly rotated after their formation. According to the model of Grasemann et al. (2003), a stable orientation of shear bands is predicted for orientations of ~30° to the foliation in general shear. According to Simpson and De Paor (1993) and Kurz and Northrup (2008), the dihedral angle between synthetic C' shear bands and the foliation corresponds to half the acute angle (ν in Eq. 1) between the flow apophyses, which is related to the vorticity number W_k by the equation:

$$\cos(\nu) = W_k \qquad (1)$$

Based on the assumption that C' shear bands lie in a stable orientation, from Eq. 1 a W_k of ~ 0.3 – 0.5 can be estimated for the Praticciolo section (Fig. 10e). The fluctuation between the calculated values (see Appendix A) is related to the uncertainties of the method rather than to vorticity changes in the shear zone (see discussion in Xypolias, 2010). As shown in Fig. 10e, antithetic C' shear bands plot at lower angles in respect to the obtuse bisector of the flow and this could indicate that they have experienced a forward rotation. This fits well with the model of Grasemann et al. (2003), which suggests that shear bands at high angle (>90°) are expected to rotate rapidly towards the fabric attractor of the flow. The recognized stable orientation of synthetic shear bands and rotation of antithetic surfaces might be interpreted as a result of C' shear band development in a stable orientation with the general zone flow during the late stage of deformation as documented by Gillam et al. (2014) in the Alpine Fault.

8. Conclusions.

We document an example of high strain domains where deformation evolved from high to low temperature conditions. An earlier high grade foliation was overprinted by several generations of shear bands marked by the retrograde growth of phyllosilicates and ductile to brittle deformation. Strain localization appears to have been mainly controlled by temperature decrease and coeval fluid circulation that favoured reaction softening and grain size reduction. Close to the brittle-ductile transition the effect of competency contrast favoured strain concentration within weak layers leaving behind fractured 'stiff' domains. The transition from ductile to brittle deformation occurred during continuous shearing, rather than due to a later brittle reactivation, leading to the extreme localization of deformation from decimetric to metric ductile shear zones into a network of discrete faults and shear fractures.

Aknowledgements

The paper greatly benefited from the thorough and constructive reviews from Florian Fusseis and Paul Bons. William Dunne is also warmly thanked for his editorial work. This work has been funded by PRA 2016 (Resp. Sergio Rocchi) of the University of Pisa.

Appendix A. Supplementary Material

Supplementary material for this article is available online.

Figure captions

Fig. 1 – Simplified geological map of southeastern Elba Island (modified after Papeschi et al., 2017). Squares highlight the location of the two studied sections. CNT: Capo Norsi thrust. CSZ: Calanchiole shear zone. FSZ: Felciaio shear zone. ZF: Zuccale fault. Mineral abbreviations: Ab: albite; And: andalusite; Bt: biotite; Crd: cordierite; Di: diopside; Wmca: white mica; Kfs: K-feldspar; Phl: phlogopite; Tr: tremolite; Wo: wollastonite.

Fig. 2 – **(a)** Simplified geological map of Capo Calvo with sample and figure location. The stereographic projection (equal angle, lower hemisphere) shows poles to the main foliation (Sp), C' shear bands and the mineral lineation (Lp). The ellipse marks the trace of the 95% confidence cone of the mean lineation vector (yellow star). Sample details are available in Appendix A. **(b-c)** Mesoscale features of Capo Calvo: **(b)** Shear band cleavage characterized by moderately east dipping C shear bands (violet arrow) that cross cut the main metamorphic foliation (Sp). Lozenges of weakly foliated andalusite-cordierite-biotite aggregates (yellow arrow) occur wrapped by the Sp. A single C' shear band (red arrow) is also visible. **(c)** Mylonitic shear zone characterized by stretched andalusite-cordierite-biotite pods (red arrow) parallel to the mylonitic foliation (Sm). Note the steeply east dipping C' shear bands that cross cut the Sm.

Fig. 3 –Microstructures of Capo Calvo taken under crossed polarizers. **(a)** Microfabric of the Sp continuous schistosity (yellow dotted line), marked by alternations of coarse grained quartz with amoeboid grain boundaries and scattered parallel biotite grains. Pinning microstructures are also present. **(b)** Detail of a coarse K-feldspar porphyroblast wrapped by the Sp foliation (yellow dotted line). The K-feldspar porphyroblast is characterized by pecilitic inclusions of biotite and coronas of sericite-biotite. **(c)** Thin section image stitching showing the contact between the oblique Sp foliation (below) and the C mylonitic foliation (above). Note the difference in grain size between the coarse-grained Sp foliation and fine-grained C shear band. Squares mark locations of Figs. 3d, e. **(d)** Detail of the oblique Sp foliation marked by alternations of biotite layers and coarse quartz ribbons with core and mantle structure. **(e)** Contact between the Sp (lower right corner) and the C shear band (top left corner) marked by the sharp decrease in grain size to fine-grained quartz, chlorite and sericite in the C shear band and the sinistral shear drag of the Sp foliation (purple arrow). **(f)** Microfabric of a quartz-rich lozenge wrapped in a C shear band. Note the oblique Sp foliation marked by the preferred orientation of both old and new, recrystallized quartz grains.
Mineral abbreviations: And: andalusite; Bt: biotite; Crd: cordierite; Kfs: K-feldspar; Qtz: quartz; Ser: sericite.

Fig. 4 – Mesoscale features of the Praticciolo area. **(a)** Simplified geological map of the Praticciolo cape with indicated location of samples and figures. Sample details are available in Appendix A. **(b)** **(above)** Photo panorama along the section marked in Fig. 4a. The southwestern side of the area is characterized by a high strain domain with mylonites, whereas in the northeastern side the dominant fabric is represented by low strain schists. Samples projected on the section are marked by green dots. **(below)** Interpreted photo panorama with lithologies coloured as in Fig. 4a.

Fig. 5 – Mesoscale structures of the Calamita Schists at the Praticciolo. **(a)** Stereographic projection (equal angle, lower hemisphere) showing poles to C' shear bands, the main foliation and mineral

lineations. The ellipse marks the trace of the 95% confidence cone of the mean lineation vector (yellow star). **(b)** Stereographic projection (equal angle, lower hemisphere) showing poles to low-angle brittle faults, Riedel Y, R1 and R2 shear fractures and brittle slickenlines. **(c)** Mylonitic fabric characterized by west dipping mylonitic foliation (Sm) with parallel quartzitic and foliated schistose bands. Asymmetric boudinage of quartzite layers occurs along C' shear bands. **(d)** Conjugate synthetic (C'1) and antithetic (C'2) C' shear bands developed in a quartz-rich lens wrapped by the Sm foliation. The inserted stereographic projection (equal angle, lower hemisphere) shows the orientation of antithetic (in red) and synthetic (in blue) C' shear bands. **(e)** Mylonitic schists with top to the east C' shear bands overprinted by top to the east Y shear fractures (red arrow). **(f)** Network of east-verging subhorizontal Y shear fractures bridged by moderately dipping R1 shear fractures that overprint the main west dipping metamorphic foliation.

Fig. 6 – Microphotographs of the Praticciolo section taken under crossed polarisers. **(a)** Alternations of lepidoblastic mica-rich domains and quartz ribbons elongated parallel to the Sm (yellow dotted line) that wraps sheared pinitized cordierite porphyroclasts. East-verging C' shear bands (red dotted line) are also visible. **(b)** Mylonitic foliation (Sm) characterized by thick alternations of coarse and fine-grained quartz ribbons and sericite layers. Nodules of sericite-chlorite represent pseudomorphs over andalusite-cordierite porphyroclasts. Note coarse quartz grains (upper left corner) mantled by finely recrystallized grains. The insert shows a detail of quartz ribbons with gypsum plate inserted highlighting the quartz CPO. **(c)** Conjugate synthetic (red arrow) and antithetic (purple arrow) C' shear fractures localized within quartz and associated with coarse chlorite grains. Note the finely recrystallized quartz and chlorite in their cores. **(d)** Synthetic dextral C' shear fractures (red arrow) localized in a coarse-grained quartz ribbon at a gentle angle in respect to the mylonitic foliation (Sm). **(e)** Detail of a very coarse (500-900 µm) quartz ribbon mantled by recrystallized quartz grains and chlorite-sericite aggregates defining the Sm. Note the conjugate C' shear fractures associated with fracturing within coarse grains (sketched in the lower

right corner) and the patchy undulose extinction of quartz. Mineral abbreviations: And: andalusite; Chl: chlorite; Crd: cordierite; Qtz: quartz; Ser: sericite; Wmca: white mica.

Fig. 7 – Microfabric of low-angle brittle faults. **(a)** Mesoscale features of the core zone of a low-angle brittle fault. A foliated ultracataclasite band (Sc = cataclastic foliation) occurs on top of unfoliated cataclasites. Note the discordant contact with both footwall and hanging wall foliation (Sp). The red rectangle highlights the sampling site of the thin section of Fig. 7b. **(b-c-d)** Microphotographs collected under crossed polarizers. **(b)** Photo stitching of the entire thin section of Fig. 7a, showing a band of unfoliated cataclasite (bottom) band of foliated ultracataclasite (middle) and the contact with the quartzite in the hanging wall (top). **(c)** Detail of the wall rock microfabric: coarse quartz grains with amoeboid grain boundaries are mantled by small bulges of tiny new grains. Red dotted lines highlight trails of recrystallized quartz grains. The yellow arrow marks a sericite-filled shear fracture. **(d)** Detail of the contact zone (cyan arrow) between the wall rock (above) and the cataclasite (below). The transition corresponds to a domain of very fine-grained quartz containing relic quartz grains with conjugate trails of recrystallized grains (purple arrow). **(e)** Microphotograph at parallel polarizers of the ultracataclasite band showing a cataclastic foliation (Sc) defined by parallel trails of angular fragments and a banded matrix with brownish phyllosilicates

Fig. 8 – Example of the analysis of dihedral angles between the Sp foliation (lower half of Fig. 9a) and C-C' shear band planes (upper half of Fig. 9a) at the Capo Calvo section (sample SP196; details in Appendix A). **(a)** Photo stitching of thin section SP196 under crossed polarisers. Three subdomains can be distinguished on a microstructural basis; the Sp domain (bottom), the Sp/C contact (centre) and the C shear band (top). **(b-c-d-e)** Rose diagrams illustrating the distribution of the Sp foliation and C-C' shear band planes. Radius lines are every 22.5° and the histogram interval is set at 5°. Inner circle interval is set at 5% of total number of measurements. The cumulative

maxima and the calculated dihedral angles are shown. See text for further details. **(b)** Sp and C orientations collected in the entire sample. **(c)** Sp and C orientations collected within the wall rock subdomain. **(d)** Sp and C orientations collected at the Sp/C contact subdomain. **(e)** C and C' orientations from the C shear band subdomain.

Fig. 9 – Sketch illustrating the evolution of mylonites in high-strain domains from peak metamorphic conditions (~650 °C) to the brittle regime (< ~300 °C). Coin for scale. **(a)** Network of white mica-bearing top to the east C shear bands that wrap lozenges bearing the high-grade Sp foliation. **(b)** Mylonite with a continuous Sm foliation consisting of mica-rich bands and stretched andalusite-cordierite-biotite pods, associated with top to the east C' shear bands. **(c)** White mica bearing mylonite with strong Sm foliation wrapping quartz-rich layers displaced by synthetic top to the east C' shear bands. **(d)** White mica bearing mylonite with quartzite boudins segmented along top to the east C' shear bands. C' shear bands have been reactivated along Y shear fractures with synthetic top to the east sense of shear. See text for discussion. (*): peak temperature for the Calamita Schists by Duranti et al., 1992. (**): temperature of chlorite bearing assemblage by Pattison and Tracy (1992). (***): brittle/ductile transition in quartz after Voll (1976).

Fig. 10 – (a) Block diagram illustrating the calculated mean orientation (expressed in dip/dip direction) of ductile and brittle structural elements and the calculated direction of the $\sigma 1$. **(b)** Example of slip tendency analysis of the Sm foliation and C' shear bands for $\mu=0.45$ and $\Delta\sigma=80$ MPa. Foliations are coloured in respect to the slip tendency Ts (Morris et al., 1996). See text for comment. **(c)** Sketched Mohr-Coulomb diagram with plotted failure envelopes for $\mu=0.7$ and $\mu=0.45$. The average orientation of C' shear bands, the Sm foliation and R1 shears in respect to $\sigma 1$ is shown in the Mohr circle. The shaded area represents orientations of pre-existing foliations that are likely to be reactivated before failure across foliation takes place. See text for details. **(d)** Failure experiment performed by Ikari et al. (2015) for a sample of Pennsylvania slate with foliation

dipping in the opposite direction to the applied shearing. At low shear strain failure across foliation takes place with the nucleation of R1 shears. Then, at higher shear strain, the main foliation is reactivated by P shears. **(e)** Rose diagram showing the orientations of synthetic and antithetic C' shear bands for the Praticciolo section in respect to the main foliation, which marks the extensional flow apophysis (A_2). The grey shaded area represents the outcrop average. Black bars denote each sample average. Black dashed lines mark the bisectors of the apophyses. The position of the contractional flow apophysis (A_1) is based on the calculations of the vorticity number W_k. See text for further details.

Table captions

Tab. 1 – Calculated mean attitude of structural elements and shear band geometries at the meso- and the microscale. Errors at 1σ.

References

Allmendinger, R. W., 2005. Stereonet. Program for stereographic projection.

Allmendinger, R. W., Marrett, R. A., Cladouhos, T., 1992. FaultKin. A program for analyzing fault slip data.

Anderson, E.M., 1951. Dynamics of Faulting and Dyke Formations with Application to Britain. Oliver & Boy, Edinburgh.

Austrheim, H., & Boundy, T. M., 1994. Pseudotachylytes generated during seismic faulting and eclogitization of the deep crust. Science 265(5168), 82-84.

Barberi, F., Innocenti, F., Ricci, C. A., 1967. Il complesso scistoso di Capo Calamita (Isola d'Elba). Atti Soc. Toscana Sci. Nat. Pisa, Mem., P.V., Ser. A 72 (2), 579–617.

Bianco, C., Brogi, A., Caggianelli, A., Giorgetti, G., Liotta, D., Meccheri, M., 2015. HP-LT metamorphism in Elba Island: Implications for the geodynamic evolution of the inner Northern Apennines (Italy). Journal of Geodynamics 91, 13-25.

Berthé, D., Choukroune, P., Gapais, D., 1979. Orientations préférentielles du quartz et orthogneissification progressive en régime cisaillant: l'exemple du cisaillement sud-armoricain. Bull. Mineral. 102, 265-272.

Bistacchi, A., Massironi, M., Menegon, L., Bolognesi, F., Donghi, V., 2012. On the nucleation of non-Andersonian faults along phyllosilicate-rich mylonite belts. Geological Society, London, Special Publications 367(1), 185-199.

Boccaletti, M., Elter, P., Guazzone, G., 1971. Plate tectonic models for the development of the Western Alps and Northern Apennines. Nature 234(49), 108-111.

Bucher, K., Grapes, R., 2011. Metamorphism of pelitic rocks (metapelites). In: Petrogenesis of Metamorphic Rocks (pp. 257-313). Springer Berlin Heidelberg.

Bukovská, Z., Jeřábek, P., Morales, L. F., 2016. Major softening at brittle-ductile transition due to interplay between chemical and deformation processes: An insight from evolution of shear bands in the South Armorican Shear Zone. Journal of Geophysical Research: Solid Earth 121(2), 1158-1182.

Butler, R.W.H., Bond, C.E., Shipton, Z.K., Jones, R.R., Casey, M., 2008. Fabric anisotropy controls faulting in the continental crust. J. Geological Soc. Lond. 165, 449–452.

Carreras, J., Czeck, D.M., Druguet, E., Hudleston, P.J., 2010. Structure and development of an anastomosing network of ductile shear zones. J. Struct. Geol. 32 (5), 656‑666.

Collettini, C., Sibson, R. H., 2001. Normal faults, normal friction? Geology 29(10), 927-930.

Collettini, C., Holdsworth, R. E., 2004. Fault zone weakening and character of slip along low-angle normal faults: insights from the Zuccale fault, Elba, Italy. Journal of the Geological Society 161(6), 1039-1051.

Collettini, C., Niemeijer, A., Viti, C., Marone, C., 2009. Fault zone fabric and fault weakness. Nature 462(7275), 907-910.

Cox, S. F., 2010. The application of failure mode diagrams for exploring the roles of fluid pressure and stress states in controlling styles of fracture-controlled permeability enhancement in faults and shear zones. Geofluids 10(1-2), 217-233.

Debenedetti, A., 1953. Osservazioni geologiche nelle zone minerarie dell'Isola d'Elba. Bollettino del Servizio Geologico d'Italia 74, 35-70.

Derez, T., Pennock, G., Drury, M., Sintubin, M., 2015. Low-temperature intracrystalline deformation microstructures in quartz. Journal of Structural Geology 71, 3-23.

Dini, A., Mazzarini, F., Musumeci, G., Rocchi, S., 2008. Multiple hydro-fracturing by boron-rich fluids in the Late Miocene contact aureole of eastern Elba Island (Tuscany, Italy). Terra Nova 20(4), 318-326.

Duranti, S., Palmeri, R., Pertusati, P. C., Ricci, C. A., 1992. Geological evolution and metamorphic petrology of the basal sequences of eastern Elba (complex II). Acta Vulcanologica 2, 213-229.

Ebert, A., Herwegh, M., Pfiffner, A., 2007. Cooling induced strain localization in carbonate mylonites within a large-scale shear zone (Glarus thrust, Switzerland). J. Struct. Geol. 29, 1164–1184.

Fossen, H., Cavalcante, G. C. G., 2017. Shear zones–A review. Earth-Science Reviews 171, 434-455.

Fusseis, F., Handy, M. R., Schrank, C., 2006. Networking of shear zones at the brittle-to-viscous transition (Cap de Creus, NE Spain). Journal of Structural Geology 28(7), 1228-1243.

Gapais, D., 1989. Shear structures within deformed granites: mechanical and thermal indicators. Geology 17(12), 1144-1147.

Gerald, J. D. F., Mancktelow, N. S., Pennacchioni, G., Kunze, K., 2006. Ultrafine-grained quartz mylonites from high-grade shear zones: Evidence for strong dry middle to lower crust. Geology 34(5), 369-372.

Gillam, B. G., Little, T. A., Smith, E., Toy, V. G., 2014. Reprint of Extensional shear band development on the outer margin of the Alpine mylonite zone, Tatare Stream, Southern Alps, New Zealand. Journal of Structural Geology 64, 115-134.

Gleason, G. C., Tullis, J., 1995. A flow law for dislocation creep of quartz aggregates determined with the molten salt cell. Tectonophysics 247(1), 1-23.

Graham, R. H., 1980. The role of shear belts in the structural evolution of the South Harris igneous complex. Journal of Structural Geology 2(1-2), 29-37.

Grasemann, B., Stüwe, K., Vannay, J. C., 2003. Sense and non-sense of shear in flanking structures. Journal of Structural Geology 25(1), 19-34.

Grohmann, C. H., Campanha, G. A., 2010. OpenStereo: open source, cross-platform software for structural geology analysis. In: AGU Fall Meeting abstracts.

Hippertt, J., Rocha, A., Lana, C., Egydio-Silva, M., Takeshita, T., 2001. Quartz plastic segregation and ribbon development in high-grade striped gneisses. Journal of Structural Geology 23(1), 67-80.

Hirth, G., Tullis, J., 1992. Dislocation creep regimes in quartz aggregates. Journal of Structural Geology 14(2), 145-159.

Hirth, G., Tullis, J., 1994. The brittle-plastic transition in experimentally deformed quartz aggregates. Journal of Geophysical Research: Solid Earth 99(B6), 11731-11747.

Holyoke, C.W., Tullis, J., 2006. Mechanisms of weak phase interconnection and the effects of phase strength contrast on fabric development. Journal of Structural Geology 28, 621-640.

Ikari, M. J., Niemeijer, A. R., Marone, C., 2015. Experimental investigation of incipient shear failure in foliated rock. Journal of Structural Geology 77, 82-91.

Jackson, J. A., Austrheim, H., McKenzie, D., Priestley, K., 2004. Metastability, mechanical strength, and the support of mountain belts. Geology 32, 625-628.

Jessell, M. W., 1987. Grain-boundary migration microstructures in a naturally deformed quartzite. Journal of Structural Geology 9(8), 1007-1014.

Jessell, M.W., Bons, P.D., Griera, A., Evans, L.A., Wilson, C.J.L., 2009. A tale of two viscosities. Journal of Structural Geology 31 (7), 719-736.

Ji, S., Jiang, Z., Rybacki, E., Wirth, R., Prior, D., Xia, B., 2004. Strain softening and microstructural evolution of anorthite aggregates and quartz‑anorthite layered composites deformed in torsion. Earth Planet. Sci. Lett. 222, 377‑390.

Keller, J. V. A., Coward, M. P., 1996. The structure and evolution of the Northern Tyrrhenian Sea. Geological Magazine 133(1), 1-16.

Kilian, R., Heilbronner, R., Stünitz, H., 2011. Quartz grain size reduction in a granitoid rock and the transition from dislocation to diffusion creep. Journal of Structural Geology 33(8), 1265-1284.

Kjøll, H. J., Viola, G., Menegon, L., Sørensen, B. E., 2015. Brittle-viscous deformation of vein quartz under fluid-rich lower greenschist facies conditions. Solid Earth 6(2), 681.

Kurz, G. A., Northrup, C. J., 2008. Structural analysis of mylonitic rocks in the Cougar Creek Complex, Oregon–Idaho using the porphyroclast hyperbolic distribution method, and potential use of SC′-type extensional shear bands as quantitative vorticity indicators. Journal of Structural Geology 30(8), 1005-1012.

Law, R. D., Knipe, R. J., Dayan, H., 1984. Strain path partitioning within thrust sheets: microstructural and petrofabric evidence from the Moine Thrust zone at Loch Eriboll, northwest Scotland. Journal of Structural Geology 6(5), 477-497.

Law, R.D., Searle, M.P., Simpson, R.L., 2004. Strain, deformation temperatures and vorticity of flow at the top of the Greater Himalayan Slab, Everest Massif, Tibet. Journal of the Geological Society of London 161, 305-320.

Little, T.A., Hacker, B.R., Gordon, S.M., Baldwin, S.L., Fitzgerald, P.G., Ellis, S., Korchinski, M., 2011. Diapiric exhumation of the world's youngest (UHP) eclogites in the gneiss domes of the D'Entrecasteaux Islands Papua New Guinea. Tectonophysics, 30.

Lister, G. S., Snoke, A. W., 1984. SC mylonites. Journal of Structural Geology 6(6), 617-638.

Logan, J. M., Dengo, C. A., Higgs, N. G., Wang, Z. Z., 1992. Fabrics of experimental fault zones: Their development and relationship to mechanical behavior. In: Evans, B., Wong, T.F., (Eds.) Fault mechanics and transport properties of rocks. New York Academic Press, pp. 33-68.

Maineri, C., Benvenuti, M., Costagliola, P., Dini, A., Lattanzi, P., Ruggieri, G., Villa, I. M., 2003. Sericitic alteration at the La Crocetta deposit (Elba Island, Italy): interplay between magmatism, tectonics and hydrothermal activity. Mineralium Deposita 38(1), 67-86.

Massa, G., Musumeci, G., Mazzarini, F., Pieruccioni, D., 2017. Coexistence of contractional and extensional tectonics during the northern Apennines orogeny: the late Miocene out-of-sequence thrust in the Elba Island nappe stack. Geological Journal 52(3), 353-368.

Massironi, M., Bistacchi, A., Menegon, L., 2011. Misoriented faults in exhumed metamorphic complexes: Rule or exception? Earth and Planetary Science Letters 307(1), 233-239.

Mazzarini, F., Musumeci, G., 2008. Hydrofracturing-related sill and dyke emplacement at shallow crustal levels: the Eastern Elba Dyke Complex, Italy. Geological Society, London, Special Publications 302(1), 121-129.

Means, W.D., 1995. Shear zones and rock history. Tectonophysics 247, 157-160.

Menegon, L., Pennacchioni, G., Heilbronner, R., Pittarello, L., 2008. Evolution of quartz microstructure and c-axis crystallographic preferred orientation within ductilely deformed granitoids (Arolla unit, Western Alps). Journal of Structural Geology 30(11), 1332-1347.

Menegon, L., Nasipuri, P., Stünitz, H., Behrens, H., & Ravna, E. (2011). Dry and strong quartz during deformation of the lower crust in the presence of melt. Journal of Geophysical Research: Solid Earth 116(B10).

Menegon, L., Stünitz, H., Nasipuri, P., Heilbronner, R., Svahnberg, H., 2013. Transition from fracturing to viscous flow in granulite facies perthitic feldspar (Lofoten, Norway). Journal of Structural Geology 48, 95-112.

Menegon, L., Pennacchioni, G., Malaspina, N., Harris, K., Wood, E., 2017. Earthquakes as precursors of ductile shear zones in the dry and strong lower crust. Geochemistry, Geophysics, Geosystems.

Morris, A., Ferrill, D. A., Henderson, D. B., 1996. Slip-tendency analysis and fault reactivation. Geology 24(3), 275-278.

Musumeci, G., Mazzarini, F., Tiepolo, M., Di Vincenzo, G., 2011. U-Pb and 40Ar-39Ar geochronology of Palaeozoic units in the northern Apennines: determining protolith age and alpine evolution using the Calamita Schist and Ortano Porphyroid. Geological Journal 46(4), 288-310.

Musumeci, G., Vaselli, L., 2012. Neogene deformation and granite emplacement in the metamorphic units of northern Apennines (Italy): Insights from mylonitic marbles in the Porto Azzurro pluton contact aureole (Elba Island). Geosphere 8(2), 470-490.

Musumeci, G., Mazzarini, F., Cruden, A. R., 2015. The Zuccale Fault, Elba Island, Italy: a new perspective from fault architecture. Tectonics 34(6), 1195-1218.

Papeschi, S., Musumeci, G., Mazzarini, F., 2017. Heterogeneous brittle-ductile deformation at shallow crustal levels under high thermal conditions: The case of a synkinematic contact aureole in the inner northern Apennines, southeastern Elba Island, Italy. Tectonophysics 717, 547-564.

Passchier, C. W., Trouw, R. A. J., 2005. Microtectonics. 2nd Edition. Springer–Verlag, Berlin.

Passchier, C., Coelho, S., 2006. An outline of shear-sense analysis in high-grade rocks. Gondwana Research 10(1), 66-76.

Pattison, D.R.M. Tracy, R.J., 1992. Phase equilibria and thermobarometry of metapelites. In: Contact Metamorphism (ed. Kerrick, D.M.), Reviews in Mineralogy 26, 105-206.

Pennacchioni, G., 2005. Control of the geometry of precursor brittle structures on the type of ductile shear zone in the Adamello tonalites, Southern Alps (Italy). Journal of Structural Geology 27(4), 627-644.

Pennacchioni, G., Mancktelow, N. S., 2007. Nucleation and initial growth of a shear zone network within compositionally and structurally heterogeneous granitoids under amphibolite facies conditions. Journal of Structural Geology, 29(11), 1757-1780.

Pennacchioni, G., Mancktelow, N. S., 2013. Initiation and growth of strike-slip faults within intact metagranitoid (Neves area, eastern Alps, Italy). Geological Society of America Bulletin 125(9-10), 1468-1483.

Pertusati, P. C., Raggi, G., Ricci, C. A., Duranti, S., Palmeri, R., 1993. Evoluzione post-collisionale dell'Elba centro-orientale. Memorie della Società Geologica Italiana 49, 297-312.

Platt, J.P., 2015. Influence of shear heating on microstructurally defined plate boundary shear zones. J. Struct. Geol. 79, 80‑89.

Platt, J. P., Vissers, R. L. M., 1980. Extensional structures in anisotropic rocks. Journal of Structural Geology 2(4), 397-410.

Ponce, C., Druguet, E., Carreras, J., 2013. Development of shear zone-related lozenges in foliated rocks. Journal of Structural Geology 50, 176-186.

Ramsay, J. G., 1980. Shear zone geometry: a review. Journal of structural geology 2(1-2), 83-99.

Ramsay, J. G., Graham, R. H., 1970. Strain variation in shear belts. Canadian Journal of Earth Sciences 7(3), 786-813.

Ramsay, J. G., Huber, M. I., 1983. Techniques of modern structural geology, Volume 1: Strain analysis. Academic Press, London.

Roper, P. J., 1972. Structural significance of "Button" or "Fish Scale" texture in phyllonitic schist of the Brevard Zone, Northwestern South Carolina. Geological Society of America Bulletin 83(3), 853-860.

Rosenberg, C. L., Stünitz, H., 2003. Deformation and recrystallization of plagioclase along a temperature gradient: an example from the Bergell tonalite. Journal of Structural Geology 25(3), 389-408.

Rutter, E. H., 1986. On the nomenclature of mode of failure transitions in rocks. Tectonophysics 122(3-4), 381-387.

Rutter, E.H., Holdsworth, R.E., Knipe, R., 2001. The nature and tectonic significance of fault-zone weakening: an introduction. Geol. Soc. Lond. Spec. Publ. 186, 1–11.

Schmid, S. M., Handy, M. R., 1991. Towards a genetic classification of fault rocks: geological usage and tectonophysical implications. In: Müller, D.W., McKenzie, J.A., Weissert, H., (Eds.) Controversies in Modern Geology, evolution of geological theories in sedimentology, earth history and tectonics. Academic Press, London, 339-361.

Schneider, C. A., Rasband, W. S., & Eliceiri, K. W., 2012. NIH Image to ImageJ: 25 years of image analysis. Nature methods 9(7), 671.

Sibson, R. H., 1977. Fault rocks and fault mechanisms. Journal of the Geological Society 133(3), 191-213.

Sibson, R. H., 1983. Continental fault structure and the shallow earthquake source. Journal of the Geological Society 140(5), 741-767.

Sibson, R. H., 1985. A note on fault reactivation. Journal of Structural Geology 7(6), 751-754.

Simpson, C., De Paor, D. G., 1993. Strain and kinematic analysis in general shear zones. Journal of Structural Geology 15(1), 1-20.

Siivola, J., Schmidt, R., 2007. List of mineral abbreviations.Recommendations by the IUGS Subcommission on the systematics of metamorphic rocks. In: Fettes, D. Desmons, J., (Eds.) Metamorphic Rocks: A Classification and Glossary of Terms. Cambridge University Press, Cambridge.

Smith, S. A. F., Holdsworth, R. E., Collettini, C., Pearce, M. A., 2011. The microstructural character and mechanical significance of fault rocks associated with a continental low-angle normal fault: the Zuccale Fault, Elba Island, Italy. Geological Society, London, Special Publications 359(1), 97-113.

Steffen, K., Selverstone, J., Brearley, A., 2001. Episodic weakening and strengthening during synmetamorphic deformation in a deep-crustal shear zone in the Alps. Geol. Soc. Lond. Spec. Publ. 186, 141‑156.

Stipp, M., Stünitz, H., Heilbronner, R., Schmid, S. M., 2002. The eastern Tonale fault zone: a 'natural laboratory' for crystal plastic deformation of quartz over a temperature range from 250 to 700 °C. Journal of Structural Geology 24(12), 1861-1884.

Stipp, M., Tullis, J., Scherwath, M., Behrmann, J. H., 2010. A new perspective on paleopiezometry: Dynamically recrystallized grain size distributions indicate mechanism changes. Geology 38(8), 759-762.

Stünitz, H., & Tullis, J., 2001. Weakening and strain localization produced by syn-deformational reaction of plagioclase. International Journal of Earth Sciences 90(1), 136-148.

Tanaka, H., 1992. Cataclastic lineations. Journal of Structural Geology 14, 1239-1252.

Trevisan, L. (1950). L'Elba orientale e la sua tettonica di scivolamento per gravità. Società Cooperativa Tipografica, Padova.

Tullis, J., Snoke, A. W., Todd, V. R., 1982. Significance and petrogenesis of mylonitic rocks. Geology 10(5), 227-230.

Viegas, G., Menegon, L., Archanjo, C., 2016. Brittle grain-size reduction of feldspar, phase mixing and strain localization in granitoids at mid-crustal conditions (Pernambuco shear zone, NE Brazil). Solid Earth 7(2), 375-396.

Voll, G., 1976. Recrystallization of quartz, biotite and feldspars from Erstfeld to the Leventina Nappe, Swiss Alps, and its geological significance. Schweiz. Mineral. Petrogr. Mitt. 56, 147.

Wallis, S., 1995. Vorticity analysis and recognition of ductile extension in the Sanbagawa belt, SW Japan. Journal of Structural Geology 17(8), 1077-1093.

White, S., 1979. Large strain deformation: report on a Tectonic Studies Group discussion meeting held at Imperial College, London on 14 November 1979. Journal of Structural Geology 1(4), 333-339.

White, S. H., Burrows, S. E., Carreras, J., Shaw, N. D., Humphreys, F. J., 1980. On mylonites in ductile shear zones. Journal of Structural Geology 2(1-2), 175-187.

Zhang, L., He, C., 2016. Frictional properties of phyllosilicate-rich mylonite and conditions for the brittle-ductile transition. Journal of Geophysical Research: Solid Earth 121(4), 3017-3047.

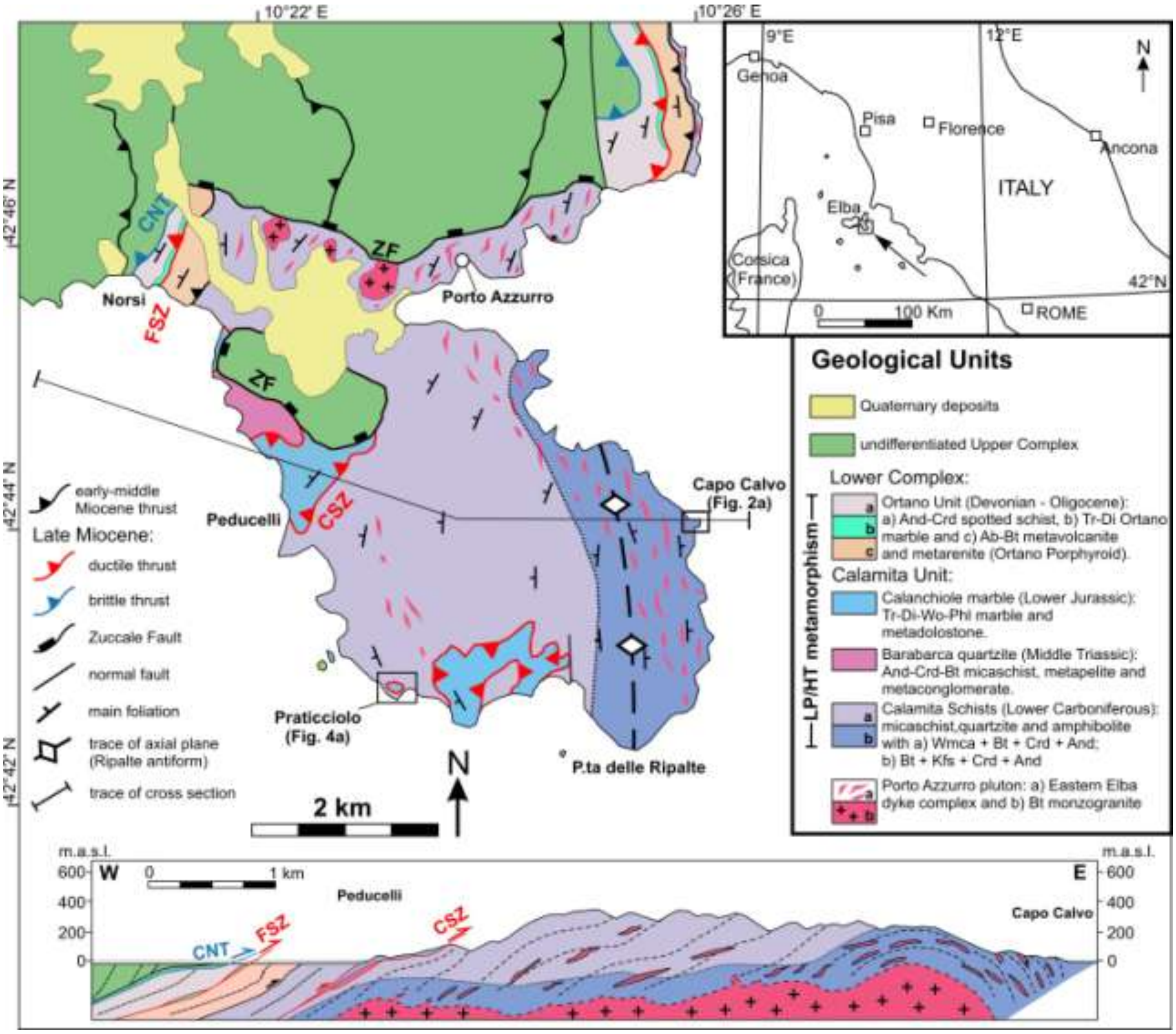

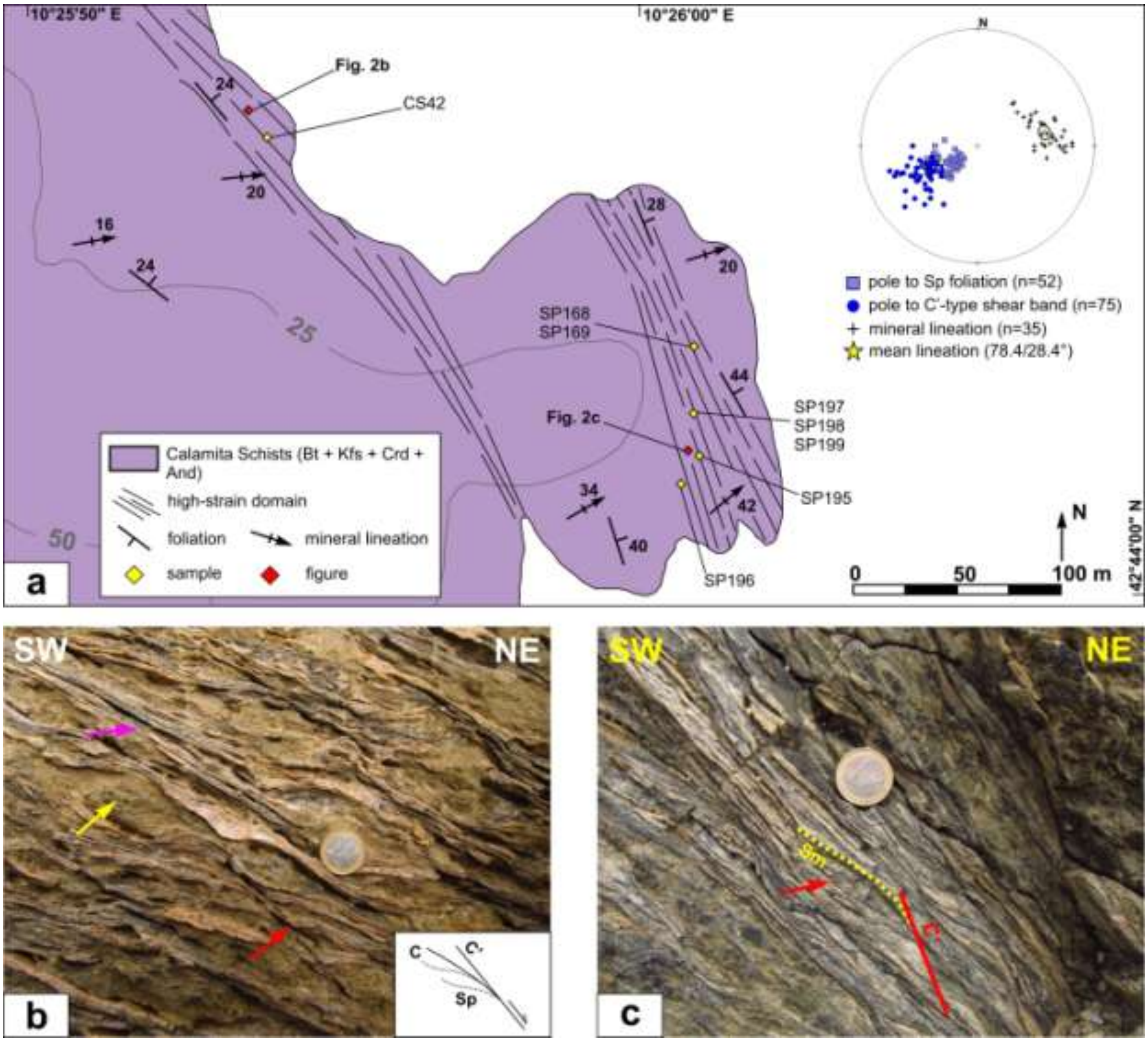

10°25'50" E
10°26'00" E
Fig. 2b
CS42
Fig. 2c
SP168
SP169
SP197
SP198
SP199
SP195
SP196
25
50
N
pole to Sp foliation (n=52)
pole to C'-type shear band (n=75)
mineral lineation (n=35)
mean lineation (78.4/28.4°)
Calamita Schists (Bt + Kfs + Crd + And)
high-strain domain
foliation
mineral lineation
sample
figure
0
50
100 m
42°44'00" N
a
SW
NE
C
C'
Sp
b
Sm
c

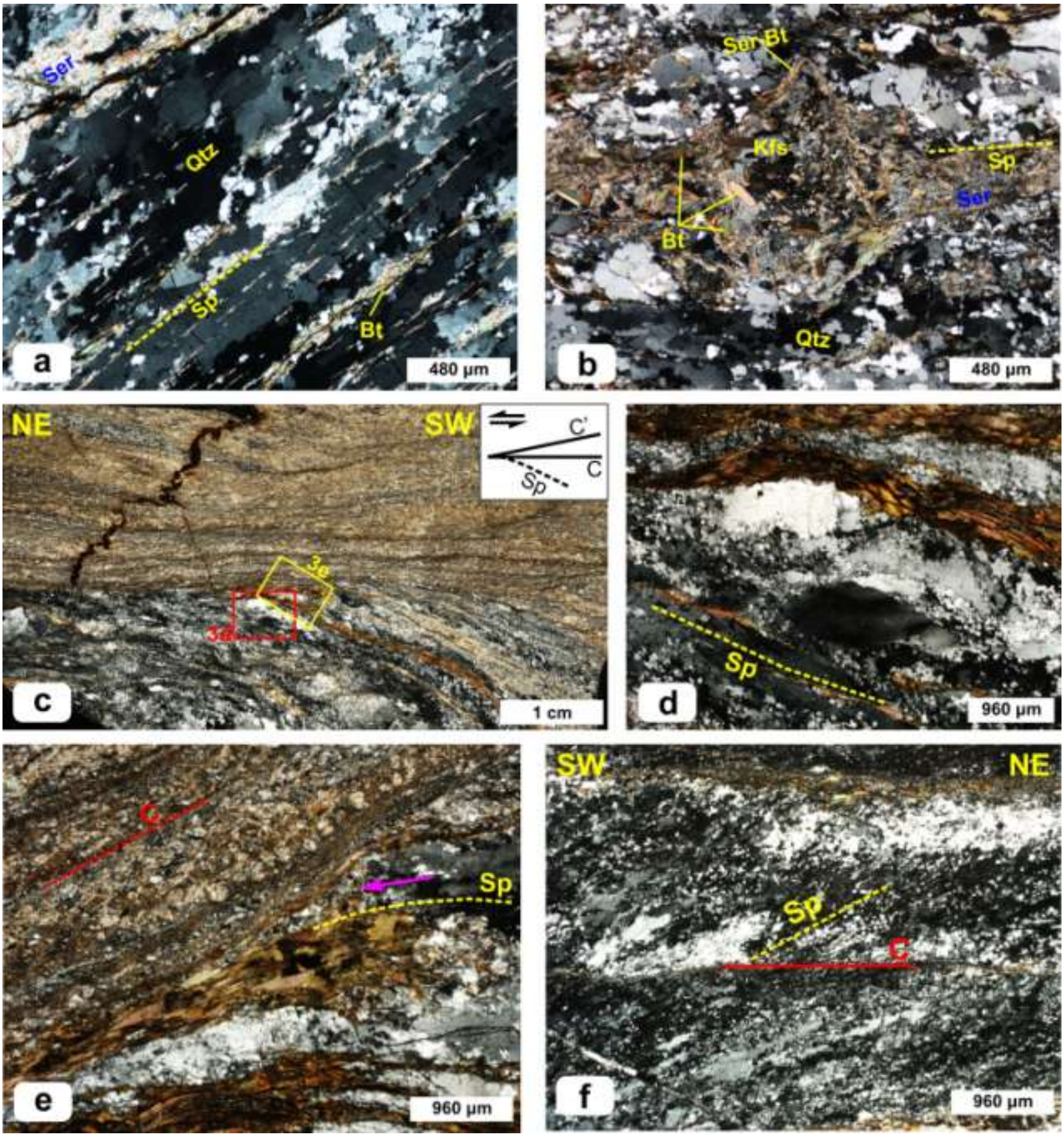
Ser
Qtz
Sp
Bt
a
480 µm
Ser-Bt
Kfs
Sp
Ser
Bt
Qtz
b
480 µm
NE
SW
C'
C
Sp
3e
3d
c
1 cm
Sp
d
960 µm
C
Sp
e
960 µm
SW
NE
Sp
C
f
960 µm

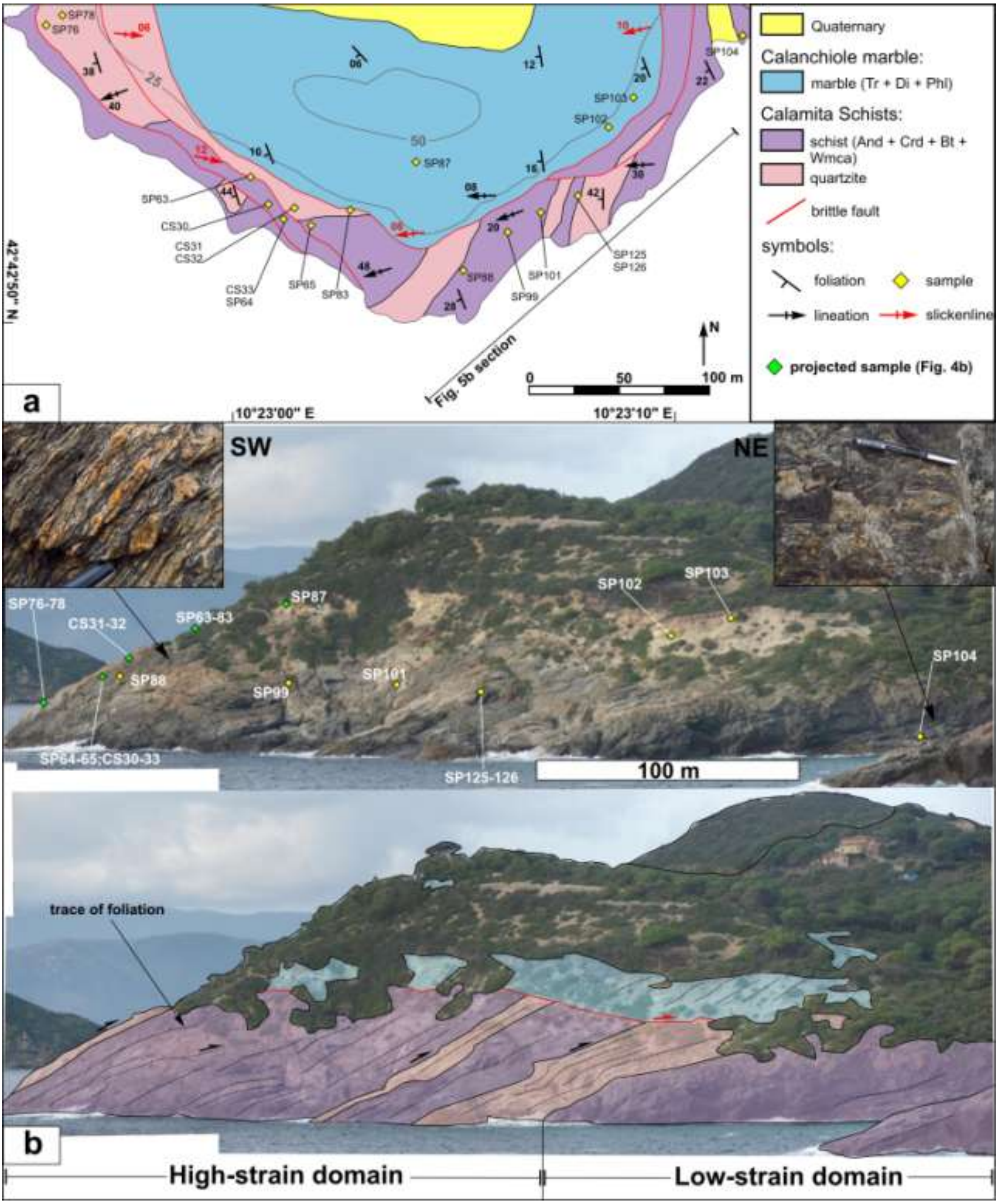
Quaternary
Calanchiole marble:
marble (Tr + Di + Phl)
Calamita Schists:
schist (And + Crd + Bt + Wmca)
quartzite
brittle fault
symbols:
foliation
sample
lineation
slickenline
projected sample (Fig. 4b)
Fig. 5b section
0
50
100 m
N
a
10°23'00" E
10°23'10" E
42°42'50" N
SP78
SP76
SP104
SP103
SP102
SP87
SP63
CS30
CS31
CS32
CS33
SP64
SP65
SP83
SP88
SP99
SP101
SP125
SP126
SW
NE
SP76-78
CS31-32
SP63-83
SP87
SP102
SP103
SP88
SP99
SP101
SP104
SP64-65;CS30-33
SP125-126
100 m
trace of foliation
b
High-strain domain
Low-strain domain

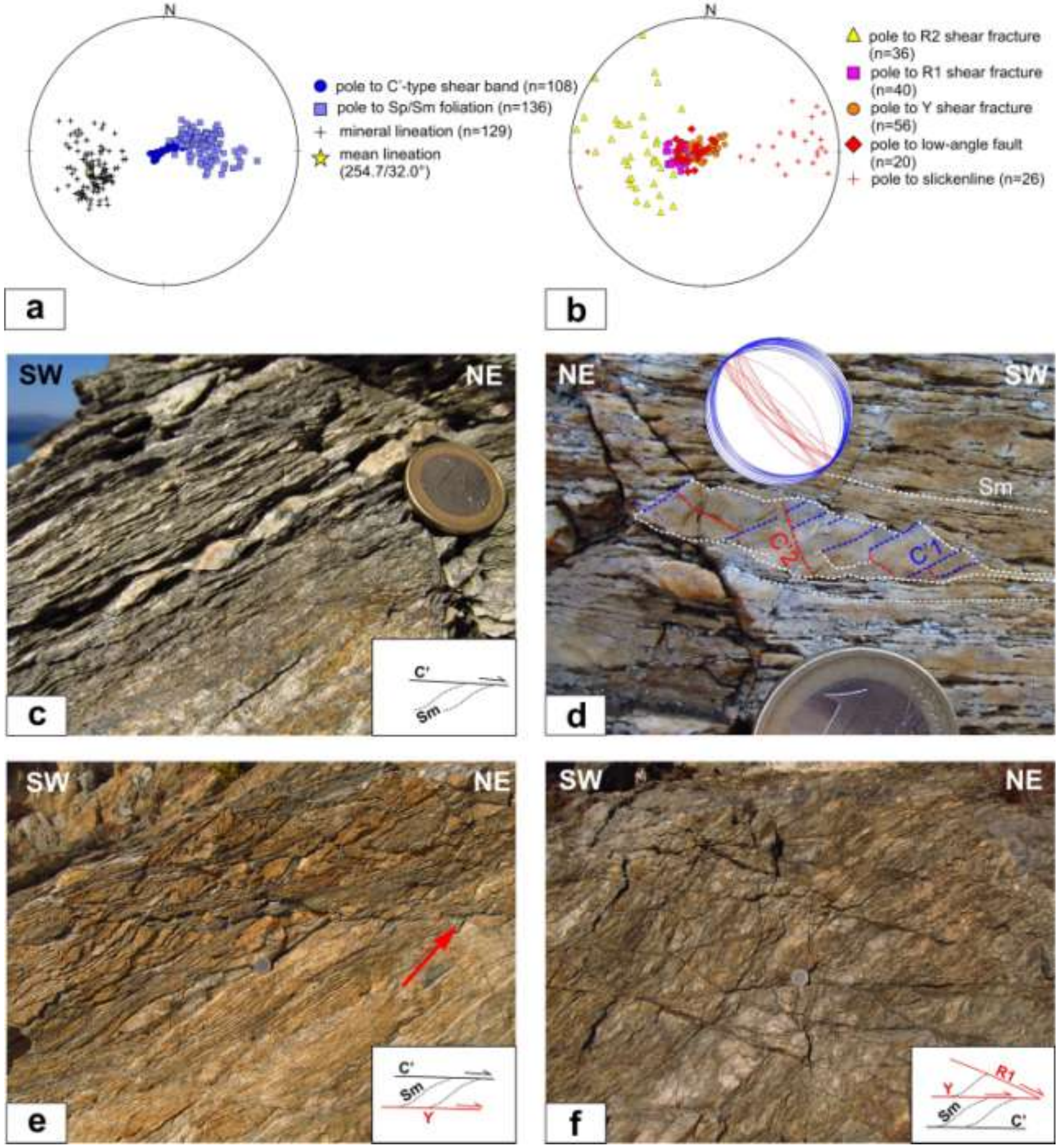
N
pole to C'-type shear band (n=108)
pole to Sp/Sm foliation (n=136)
mineral lineation (n=129)
mean lineation
(254.7/32.0°)
a
N
pole to R2 shear fracture
(n=36)
pole to R1 shear fracture
(n=40)
pole to Y shear fracture
(n=56)
pole to low-angle fault
(n=20)
pole to slickenline (n=26)
b
SW
NE
C'
Sm
c
NE
SW
Sm
C'2
C'1
d
SW
NE
C'
Sm
Y
e
SW
NE
R1
Y
Sm
C'
f

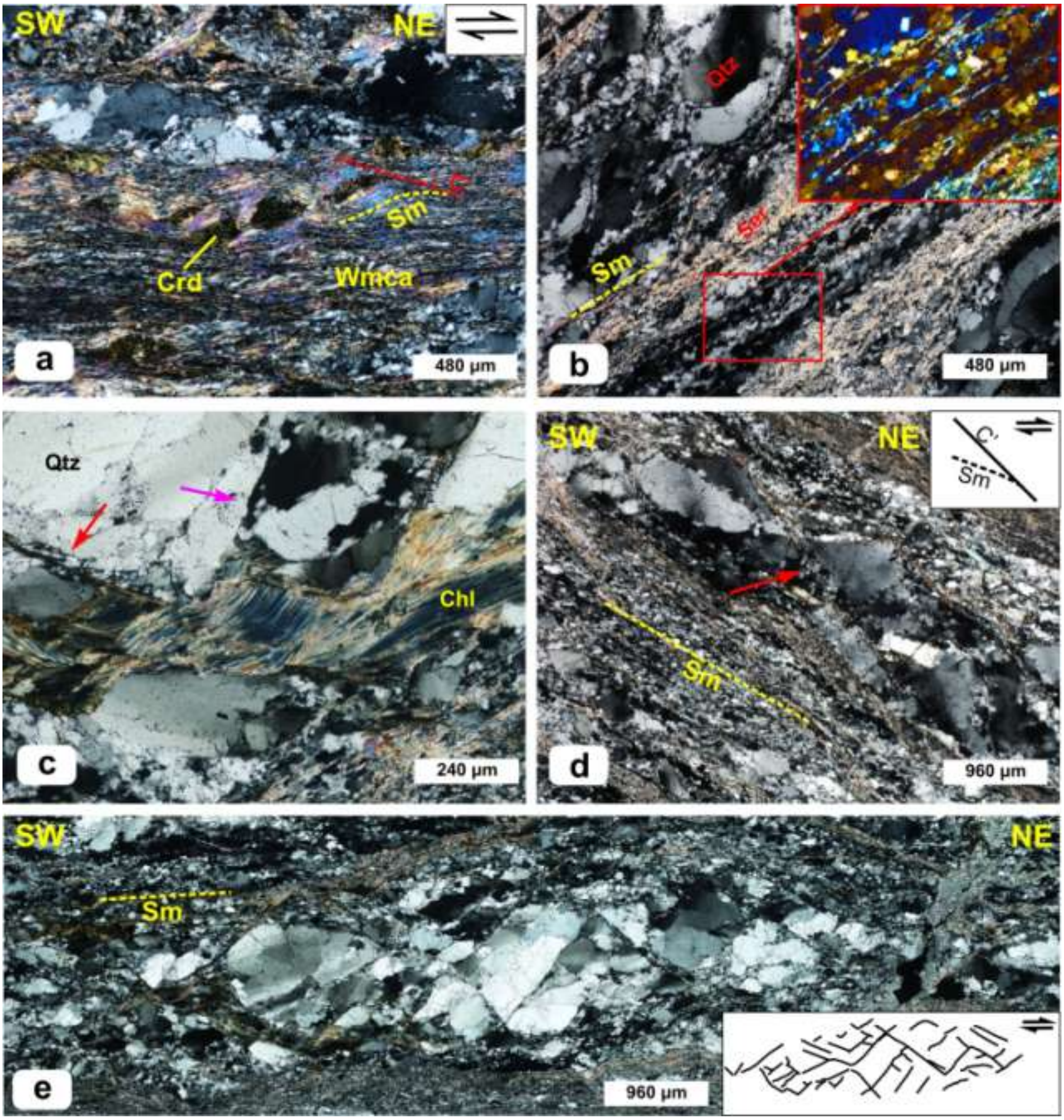

SW
NE
C'
Sm
Crd
Wmca
a
480 µm
Qtz
Ser
Sm
b
480 µm
Qtz
Chl
c
240 µm
SW
NE
C'
Sm
Sm
d
960 µm
SW
NE
Sm
e
960 µm

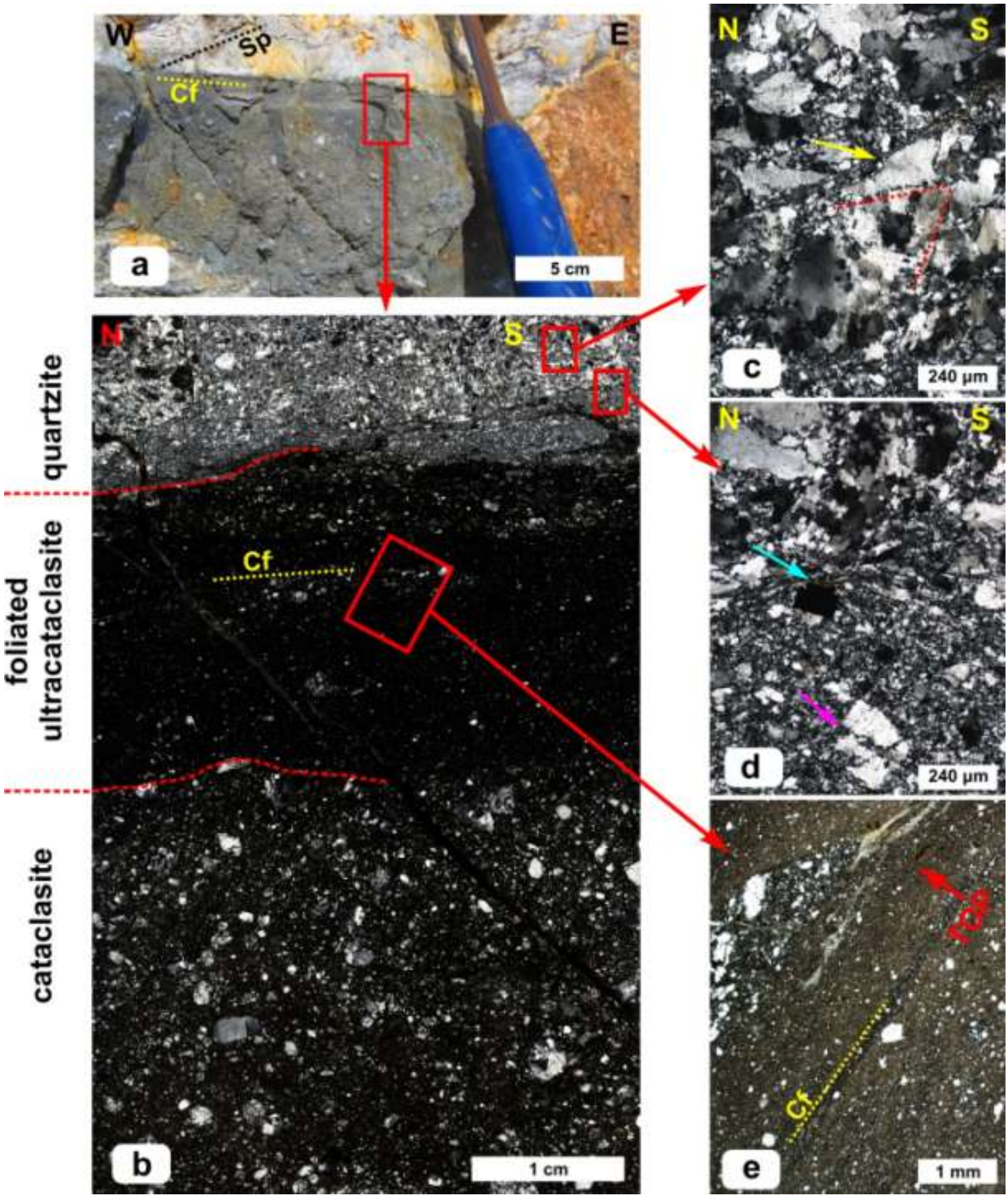

W
E
Sp
Cf
a
5 cm
N
S
quartzite
foliated ultracataclasite
cataclasite
Cf
b
1 cm
N
S
c
240 µm
N
S
d
240 µm
Top
Cf
e
1 mm

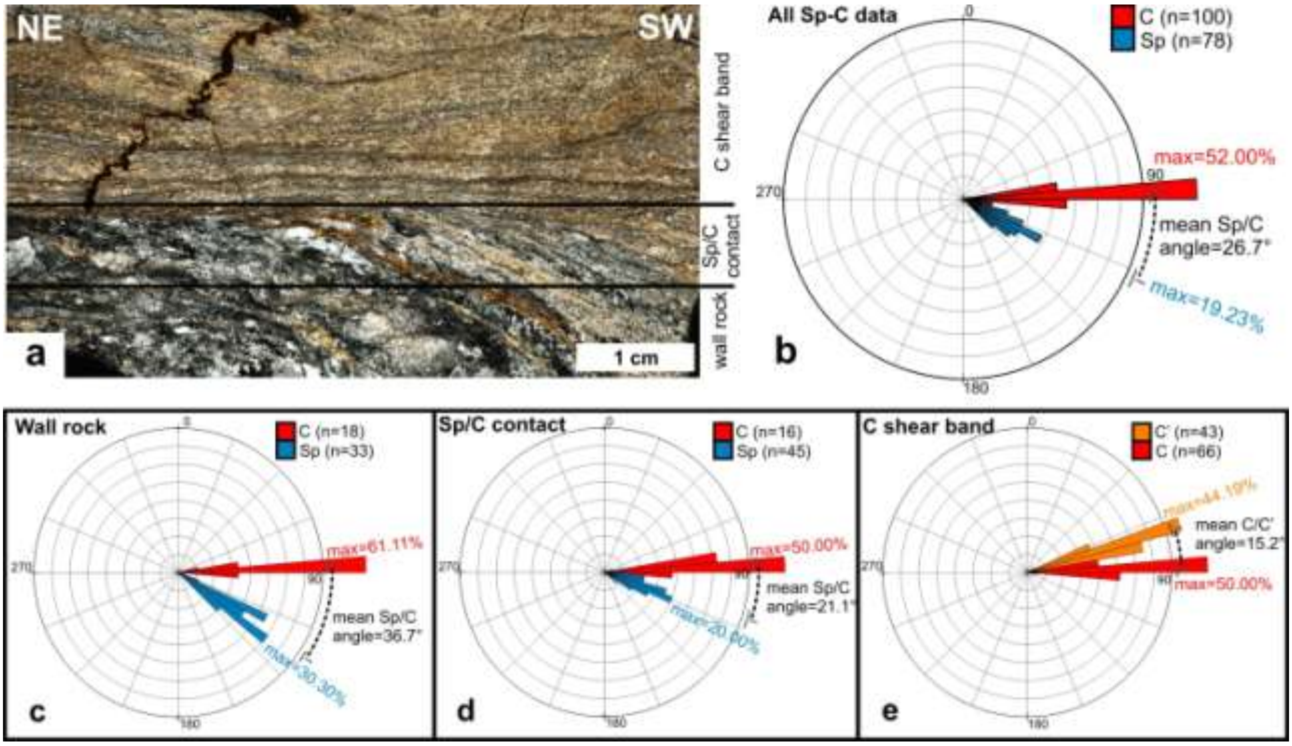

NE
SW
C shear band
Sp/C contact
wall rock
1 cm
a
All Sp-C data
C (n=100)
Sp (n=78)
max=52.00%
mean Sp/C angle=26.7°
max=19.23%
b
Wall rock
C (n=18)
Sp (n=33)
max=61.11%
mean Sp/C angle=36.7°
max=30.30%
c
Sp/C contact
C (n=16)
Sp (n=45)
max=50.00%
mean Sp/C angle=21.1°
max=20.00%
d
C shear band
C' (n=43)
C (n=66)
max=44.19%
mean C/C' angle=15.2°
max=50.00%
e

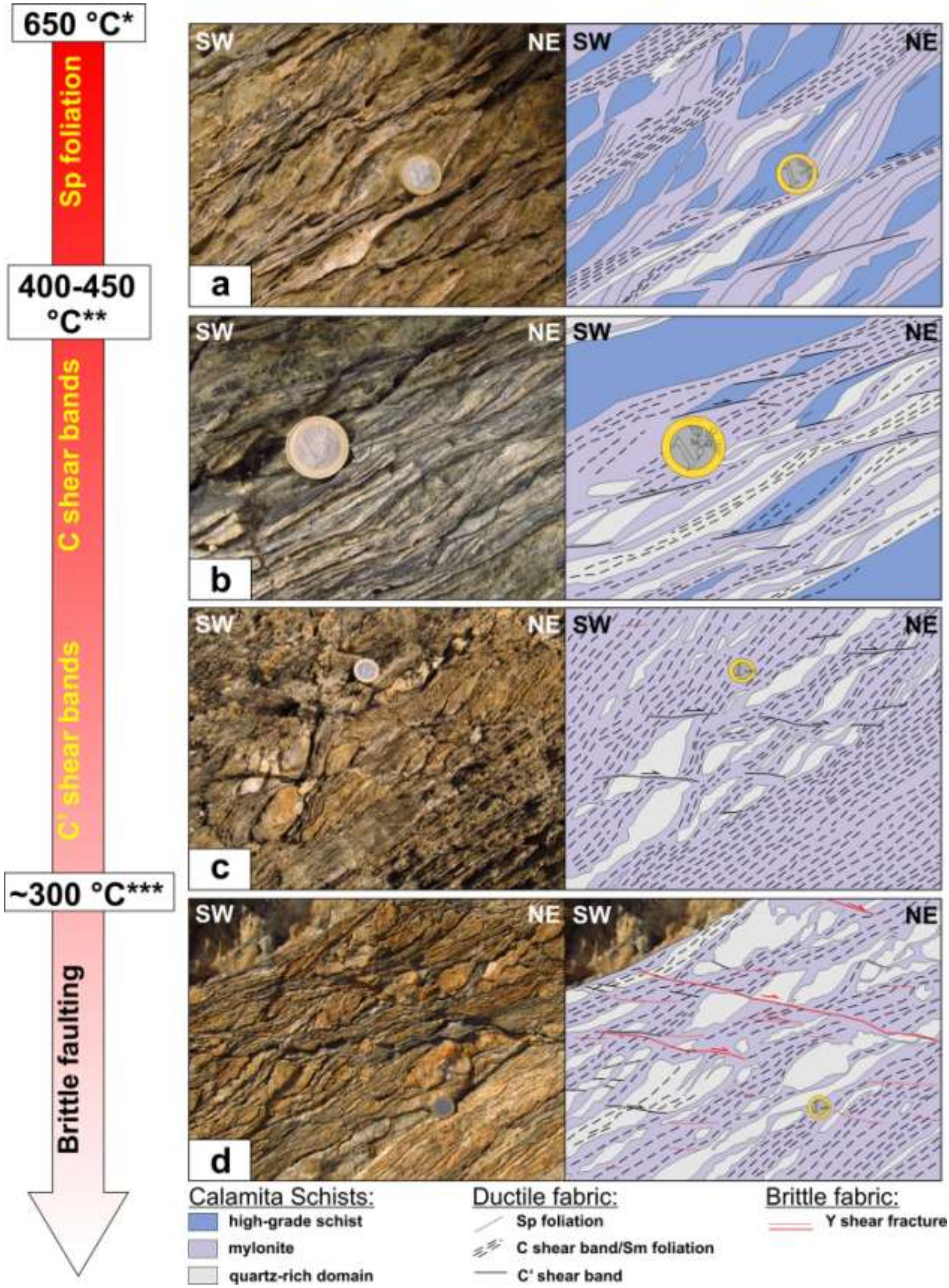
650 °C*
Sp foliation
400-450 °C**
C shear bands
C' shear bands
~300 °C***
Brittle faulting
SW
NE
a
b
c
d
Calamita Schists:
high-grade schist
mylonite
quartz-rich domain
Ductile fabric:
Sp foliation
C shear band/Sm foliation
C' shear band
Brittle fabric:
Y shear fracture

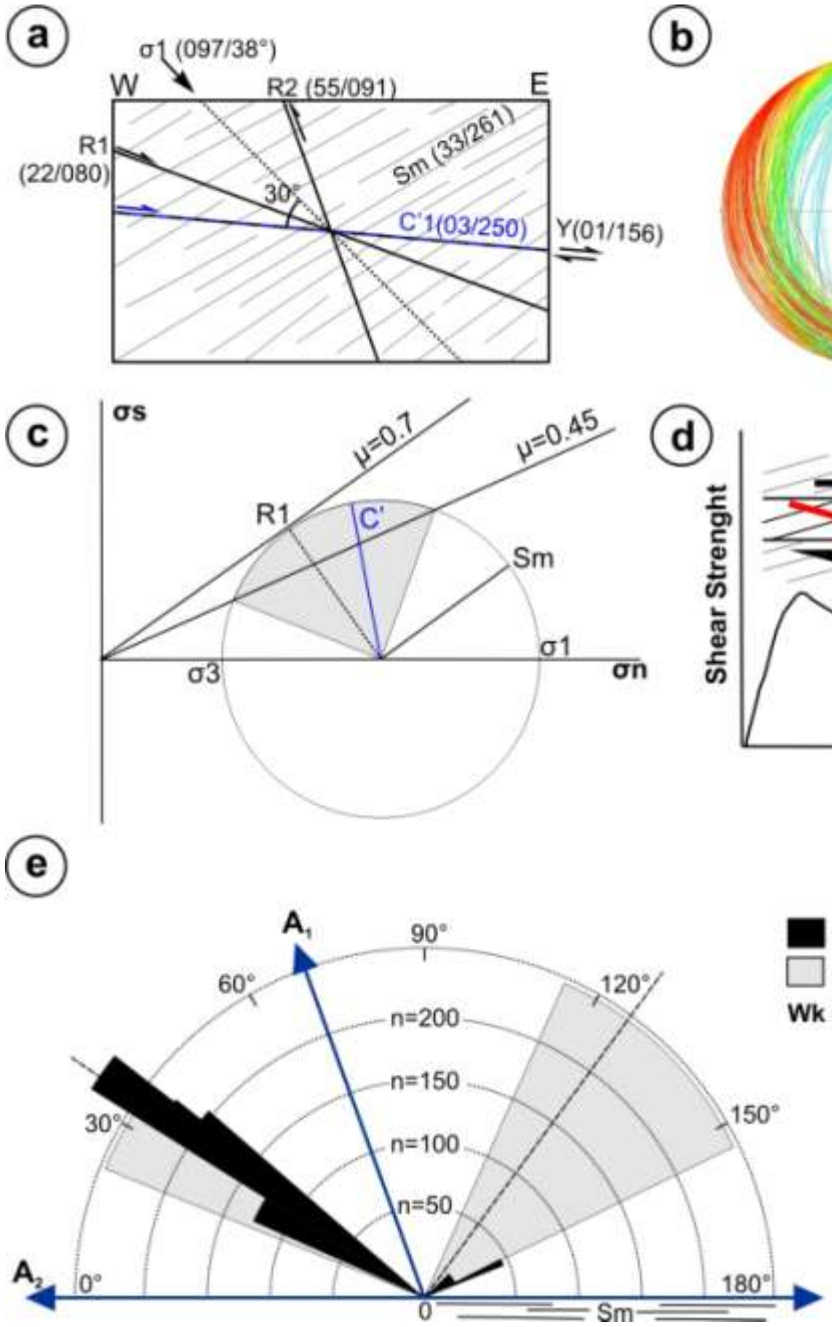
a
σ1 (097/38°)
W
E
R2 (55/091)
R1
(22/080)
Sm (33/261)
30°
C'1(03/250)
Y(01/156)
b
Δσ=80 MPa
μ=0.45
n=243
Ts
min
max
c
σs
μ=0.7
μ=0.45
R1
C'
Sm
σ1
σ3
σn
d
foliation
Y
R1
P
Shear Strenght
Ikari et al. (2015)
Shear Strain
e
A1
90°
60°
120°
n=200
n=150
n=100
n=50
30°
150°
A2
0°
180°
0
Sm
Sample average
Outcrop average
Wk = 0.37±0.05